Springer Theses
Recognizing Outstanding Ph.D. Research

Jason Leonard

Exciton Transport Phenomena in GaAs Coupled Quantum Wells

Springer

Springer Theses

Recognizing Outstanding Ph.D. Research

Aims and Scope

The series "Springer Theses" brings together a selection of the very best Ph.D. theses from around the world and across the physical sciences. Nominated and endorsed by two recognized specialists, each published volume has been selected for its scientific excellence and the high impact of its contents for the pertinent field of research. For greater accessibility to non-specialists, the published versions include an extended introduction, as well as a foreword by the student's supervisor explaining the special relevance of the work for the field. As a whole, the series will provide a valuable resource both for newcomers to the research fields described, and for other scientists seeking detailed background information on special questions. Finally, it provides an accredited documentation of the valuable contributions made by today's younger generation of scientists.

Theses are accepted into the series by invited nomination only and must fulfill all of the following criteria

- They must be written in good English.
- The topic should fall within the confines of Chemistry, Physics, Earth Sciences, Engineering and related interdisciplinary fields such as Materials, Nanoscience, Chemical Engineering, Complex Systems and Biophysics.
- The work reported in the thesis must represent a significant scientific advance.
- If the thesis includes previously published material, permission to reproduce this must be gained from the respective copyright holder.
- They must have been examined and passed during the 12 months prior to nomination.
- Each thesis should include a foreword by the supervisor outlining the significance of its content.
- The theses should have a clearly defined structure including an introduction accessible to scientists not expert in that particular field.

More information about this series at http://www.springer.com/series/8790

Jason Leonard

Exciton Transport Phenomena in GaAs Coupled Quantum Wells

Doctoral Thesis accepted by
University of California, San Diego
La Jolla, California, USA

Springer

Jason Leonard
University of California, San Diego
La Jolla, CA, USA

ISSN 2190-5053 ISSN 2190-5061 (electronic)
Springer Theses
ISBN 978-3-319-69732-1 ISBN 978-3-319-69733-8 (eBook)
https://doi.org/10.1007/978-3-319-69733-8

Library of Congress Control Number: 2017956710

© Springer International Publishing AG 2018
This work is subject to copyright. All rights are reserved by the Publisher, whether the whole or part of the material is concerned, specifically the rights of translation, reprinting, reuse of illustrations, recitation, broadcasting, reproduction on microfilms or in any other physical way, and transmission or information storage and retrieval, electronic adaptation, computer software, or by similar or dissimilar methodology now known or hereafter developed.
The use of general descriptive names, registered names, trademarks, service marks, etc. in this publication does not imply, even in the absence of a specific statement, that such names are exempt from the relevant protective laws and regulations and therefore free for general use.
The publisher, the authors and the editors are safe to assume that the advice and information in this book are believed to be true and accurate at the date of publication. Neither the publisher nor the authors or the editors give a warranty, express or implied, with respect to the material contained herein or for any errors or omissions that may have been made. The publisher remains neutral with regard to jurisdictional claims in published maps and institutional affiliations.

Printed on acid-free paper

This Springer imprint is published by Springer Nature
The registered company is Springer International Publishing AG
The registered company address is: Gewerbestrasse 11, 6330 Cham, Switzerland

Supervisor's Foreword

The thesis of Jason Leonard addresses indirect excitons (IXs). These specially designed quasiparticles give the opportunity to study fundamental properties of quantum degenerate Bose gases in semiconductors and to develop optoelectronic devices where excitons are used in place of electrons.

An IX is a bound pair of an electron and a hole confined in separate layers in a semiconductor structure. The spatial separation between the electron and hole layers allows one to control the overlap of electron and hole wave functions and engineer structures with long IX lifetime, orders of magnitude longer than the lifetime of regular direct excitons. The long lifetimes allow IXs to cool below the temperature of quantum degeneracy. This gives the opportunity to study low-temperature states in cold excitons—cold bosons in semiconductor materials. The findings in cold IXs include a spontaneous transition into a spatially modulated exciton state, spontaneous coherence and condensation of excitons, long-range spin currents and spin textures, and other transport and optical phenomena. Some of the observed phenomena, like spontaneous coherence and condensation of excitons, were theoretically predicted and some of them, like spontaneous transition into a spatially modulated exciton state, were found experimentally in a cold IX gas.

The long IX lifetimes also allow IXs to travel over large distances before recombination. This provides the opportunity to study exciton transport and spin transport by optical imaging. A set of exciton transport phenomena has been observed, including the inner ring in exciton emission patterns, exciton localization-delocalization transition in random potentials, lattices, and moving potentials, coherent exciton transport with suppressed scattering, and spin transport and spin textures.

The energy of IXs can be controlled by applied electric field. This gives the opportunity to create in-plane potential landscapes for IXs by voltage. Advantages of electrostatically created potential landscapes include the opportunity to realize a desired in-plane potential profile and control it by voltage in situ, i.e. on a time scale shorter than the IX lifetime. IXs were studied in a variety of electrostatic traps, in periodic potentials including static and moving electrostatic lattices, ramps, and narrow channels.

Besides forming a platform for studying basic physics of bosons in semiconductors, excitons can also be explored for the development of signal processing based on computational state variables beyond magnetism and charge. Excitonic devices are potentially well suited to the development of an alternative to electronics due to the opportunity to realize energy-efficient computation with efficient coupling to optical communication. The possibility to control of IX energy, fluxes, and emission rate by voltage, light, and IX interaction makes IXs suitable for the development of excitonic signal processing devices.

The thesis of Jason presents both the studies of fundamental exciton phenomena and the development of excitonic devices. In particular, the thesis describes the observation of IX spin transport, the observation of the dynamical localization-delocalization transition for excitons, the development of excitonic ramp, the development of excitonic conveyer, and the development of optically controlled excitonic transistor. The results are of interest to students and scientists working in optics, condensed matter physics, and physics of cold gases.

University of California, San Diego
September, 2017

Leonid Butov

Acknowledgements

I would like to thank my advisor Leonid Butov. Without his support and encouragement this work would not have been possible. I would also like to thank him for teaching me to think simply without sacrificing rigor and improving my communication skills.

I'd like to thank Sen Yang for training me in lab; he is remarkably patient. I'd like to thank Aaron Hammack for the many physics discussions we had. I'd like to thank Alex High for working with me on interference measurements and helping me learn to think though problems. I'd like to thank Alex Winbow for giving me a greater appreciation for experimental equipment. I'd like to thank Yuliya Kuznetsova and Mikas Remeika for the help they gave me on many experiments. I'd also like to thank Yuliya for reading the draft of my dissertation and giving me helpful feedback.

I'd like to thank Denis Scalbert, Masha Vladimirova, Steeve Cronenberger, Marion Riche, and Sergueï Andreev for helping me feel at home when I spent time in France. I'd like to thank Masha for the many physics and programming discussions we had. I'd like to thank Denis and Steeve for teaching me about time resolved reflection and Kerr rotation measurements.

I'd like to thank Peristera Andreakou for being a good friend and the many lab discussions we had.

I'd like to thank my parents for the constant support and encouragement they provided.

Contents

Parts of this thesis have been published in the following articles:

1. J. R. Leonard, M. Remeika, M. K. Chu, Y. Y. Kuznetsova, A. A High, L. V. Butov, J. Wilkes, M. Hanson, and A. C. Gossard, "Transport of Indirect Excitons in a Potential Energy Gradient," *Appl. Phys. Lett.* **100**, 231106 (2012).
2. P. Andreakou, S. V. Poltavtsev, J. R. Leonard, E. V. Calman, M. Remeika, Y. Y. Kuznetsova, L. V. Butov, J. Wilkes, M. Hanson, A. C. Gossard, "Optically controlled excitonic transistor," *Appl. Phys. Lett.* **104**, 091101 (2014).
3. A. G. Winbow, J. R. Leonard, M. Remeika, Y. Y. Kuznetsova, A. A. High, A. T. Hammack, L. V. Butov, J. Wilkes, A. A. Guenther, A. L. Ivanov, M. Hanson, and A. C. Gossard, "Electrostatic Conveyer for Excitons," *Phys. Rev. Lett.* **106**, 196806 (2011).
4. J. R. Leonard, Y. Y. Kuznetsova, Sen Yang, L. V. Butov, T. Ostatnicky, A. Kavokin, and A. C. Gossard, "Spin Transport of Excitons," *Nano Lett.* **9**, 4204 (2009).

Chapter 1
Introduction

Computers use electrical interconnects to transfer information between the processor and memory. As processor speeds have increased the speed of processor to memory and chip to chip interconnects has increased. There are a variety of tradeoffs that limit the effectiveness of electrical interconnects. One solution is to use optical interconnects, optical connections do not have the same inherent limitations as electrical connections. However, there are a variety of difficulties involved in building optical interconnects that need to be addressed (Young et al. 2010). Traditional optics such as VCSELs and resonant cavities address many of these issues, however are size limited by the wavelength of light and do not scale to the size of electrical components. Spatially indirect excitons composed of an electron and hole offer a unique system that is both optically active and electrically controllable. Indirect excitons effectively eliminate the conversion time between electrical and optical signals and are smaller than other optical devices making them a candidate system for optical interconnects (High et al. 2008; Baldo and Stojanović 2009).

To develop the building blocks of optical interconnects there are a variety of excitonic devices that control potential energy landscapes for excitons, exciton fluxes, emission rates, and other exciton characteristics. The development of excitonic devices that control exciton fluxes is mainly concentrated on indirect excitons in coupled quantum wells (CQW) (Hagn et al. 1995; Gärtner et al. 2006; High et al. 2007, 2008, 2009; Grosso et al. 2009; Remeika et al. 2009, 2012; Vögele et al. 2009; Kuznetsova et al. 2010; Cohen et al. 2011; Winbow et al. 2011; Schinner et al. 2011; Leonard et al. 2012) and exciton-polaritons in microcavities (Amo et al. 2010; Gao et al. 2012; Ballarini et al. 2013; Nguyen et al. 2013; Sturm et al. 2014).

Beyond being interesting for optical interconnects, indirect excitons carry an intrinsic angular momentum or spin. Building devices that use spin transport may offer advantages in dissipation, size, and speed over charge based devices, leading to considerable interest in the development of semiconductor electronic and excitonic devices based on spin transport; see Awschalom and Flatté (2007)

J. Leonard, *Exciton Transport Phenomena in GaAs Coupled Quantum Wells*,
Springer Theses, https://doi.org/10.1007/978-3-319-69733-8_1

and the references therein. In addition to device applications there is a variety of fundamental spin phenomena in semiconductors, including a number of interesting phenomena in electron transport, such as current-induced spin orientation (the spin Hall effect) (D'yakonov and Perel' 1971a; Hirsch 1999; Sih et al. 2005), spin-induced contribution to the current (D'yakonov and Perel' 1971b), spin injection (Aronov and Pikus 1976), and spin diffusion and drag (Dzhioev et al. 1997; Kikkawa and Awschalom 1999; D'Amico and Vignale 2001; Weber et al. 2005; Carter et al. 2006; Appelbaum et al. 2007).

1.1 Semiconductor Introduction

When atoms are combined in a periodic structure, the electronic orbitals of each atom are modified and become bands. Each band is characterized by a dispersion relationship—the relationship between momentum and energy for particles in that band. A semiconductor is a material where the Fermi level is between the conduction band and valence band. This allows the Fermi energy to be moved up into the conduction band or down into the valence band through doping or gate-voltages, manipulating the material conductivity, for details on band structure, see Kittel (2005). Silicon is used in computers because it has a high electron and hole mobility which is important for CMOS devices. Silicon is an indirect band gap semiconductor which means the minimum of the conduction band does not align with the maxima of the valence band. In order for an electron to optically decay from the conduction band to the valence band the electron must emit a phonon to conserve momentum. This gives an excited electron in silicon a very long lifetime and the material is considered optically inactive. In contrast, GaAs is a direct band gap semiconductor, so an electron can optically decay from the conduction to valence band without also emitting a phonon, see Fig. 1.1. This limits exciton lifetime and the material is considered optically active and suitable for optical applications. This dissertation focuses on GaAs exciton based devices.

1.1.1 Bulk GaAs

When GaAs absorbs a photon an electron is excited from the valence band into the conduction band. The empty location in the valence band can move (when a different electron fills that location) and has positive charge. For practical purposes this empty location in the valence band acts like a positively charged particle called a hole. Since the electron and hole have opposite charge they are attracted to each other and can form a bound state called an exciton. This is analogous to positronium. Figure 1.1 shows the band structure of bulk GaAs. Orbital angular momentum and spin are coupled together, so the bands are described in terms of $\vec{J} = \vec{L} + \vec{S}$, where

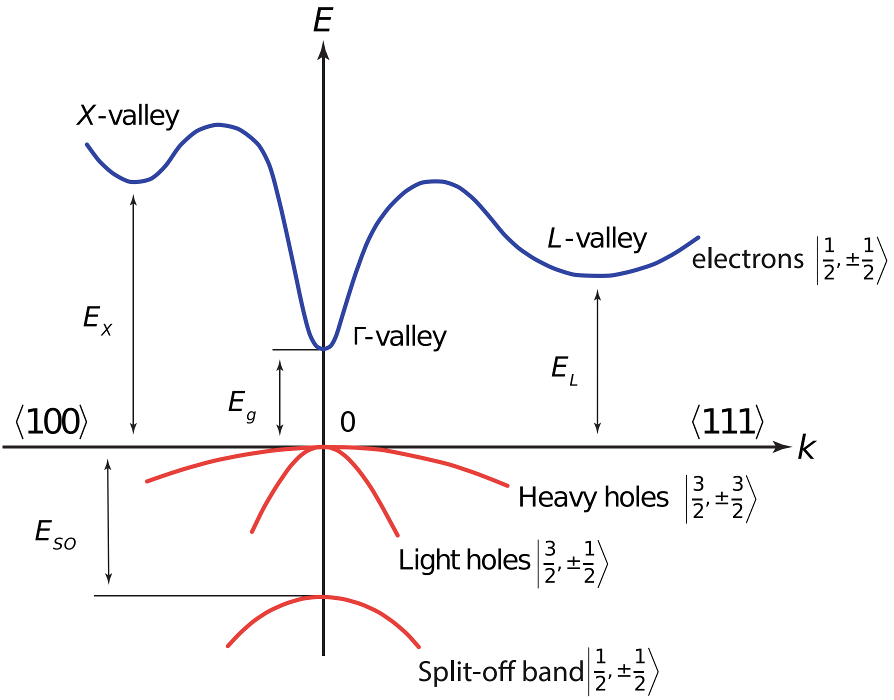

Fig. 1.1 Bulk GaAs Band Diagram. GaAs is a direct band gap semiconductor which means the minimum of the conduction band and the maximum of the valence band both occur at $k = 0$. The alignment of the extrema of the conduction and valence band allows an electron to decay into the valence band without coupling to phonon making the material optically active

$\vec{L}$ is the orbital angular momentum and $\vec{S}$ is the intrinsic angular momentum. Spin-orbit coupling causes an energy difference between $j = 1/2$ and $j = 3/2$ states in the valence band.

1.1.2 Single Quantum Well

A quantum well is a thin layer of material with a lower band-gap than the surrounding material, restricting electrons and holes to the plane of the quantum well. In a single quantum well an exciton has a lifetime on the order of tens of picoseconds (Feldmann et al. 1987; Andreani et al. 1991; Deveaud et al. 1991). Confinement along the z-axis modifies the structure of the $j = 3/2$ band. In bulk GaAs, holes with $j = 3/2$ are degenerate near $k = 0$. In quantum wells, there is a $k = 0$ energy splitting between $m_j = \pm 3/2$ and $m_j = \pm 1/2$ holes (Fig. 1.2) (Yu and Cardona 2005). In general, this splitting does not directly affect the results in this dissertation. However, the coupled quantum well absorbtion spectrum shows two

Fig. 1.2 GaAs single quantum well valence band diagram. The energy difference at $k = 0$ is due to confinement in the z-direction. Due to the low lattice temperature indirect excitons consist primarily of heavy holes

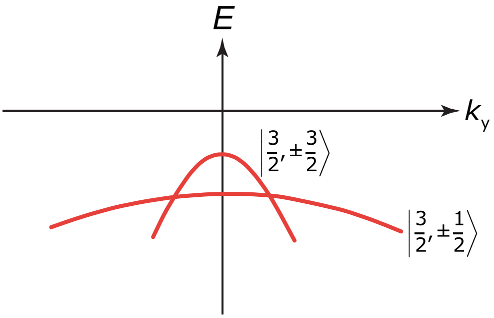

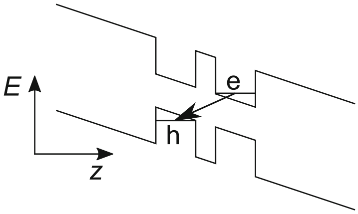

Fig. 1.3 Indirect Exciton Band Diagram. Energy diagram showing coupled quantum wells with an applied electric field along the z-axis. Arrow indicates the electron and hole are in a bound state. Electrons will move to the lower energy quantum well, holes to the higher energy quantum well. The quantum wells are positioned near each other so the electron and hole can bind together into an exciton. The spatial separation results in a large increase of exciton lifetime

peaks corresponding to excitons containing a light-/heavy-hole. The spin physics of the system changes depending on which resonance is excited. Both of these effects were measured in Leonard et al. (2008). For details about the effect of the HH/LH splitting on exciton spin dynamics, see Viña (1999).

1.1.3 Coupled Quantum Wells

In this case, coupled means the quantum wells are placed close enough that particles in one well can interact with particles in the other well. A voltage is applied perpendicular to the plane of the quantum wells. This “gate-voltage” changes the energies of the two wells so that electrons go into one of the wells and holes go into the other well, see Fig. 1.3. The structure is designed so that electrons in one well bind to holes in the other well. These bound particles are called indirect excitons. This design gives rise to many of an indirect exciton’s unique properties such as a long lifetime, a long spin lifetime, a large transport distance, and in situ control. In this dissertation, I explore several devices based on these properties.

1.1.3.1 Long Lifetime

The spatial separation allows one to control the overlap of electron and hole wavefunctions and engineer structures with lifetimes of indirect excitons orders of magnitude longer than those of direct excitons. Indirect excitons considered in this dissertation have lifetimes on the order of tens of nanoseconds compared to direct excitons with lifetimes on the order of tens of picoseconds (Feldmann et al. 1987; Andreani et al. 1991; Deveaud et al. 1991; Butov et al. 1999; Hammack et al. 2009).

1.1.3.2 Long Spin Lifetime

Indirect excitons have a long spin lifetime compared to direct excitons. The long spin lifetime results from the suppression of the electron–hole exchange interaction by the spatial separation of the electron and hole wavefunctions. Spin physics are detailed in Sect. 1.3.

1.1.3.3 Long Transport Distance

Long lifetimes of indirect excitons allow them to travel over macroscopic distances before recombination (Hagn et al. 1995; Butov and Filin 1998; Larionov et al. 2000; Butov et al. 2002; Vörös et al. 2005; Ivanov et al. 2006; Gärtner et al. 2006; Hammack et al. 2009; Alloing et al. 2011, 2012).

1.1.3.4 In Situ Control

Indirect excitons have a built-in dipole moment ed, where d is close to the distance between the quantum well centers, that allows their energy to be controlled by voltage: an electric field F_z perpendicular to the quantum well plane results in the exciton energy shift $E = edF_z$ (Miller et al. 1985). This property is used to create electrostatic in-plane potential landscapes $E(x, y) = edF_z(x, y)$.

Exciton transport was studied in various electrostatic potential landscapes including circuit devices (High et al. 2007, 2008; Grosso et al. 2009), traps (High et al. 2009), lattices (Remeika et al. 2009, 2012), narrow channels (Vögele et al. 2009; Grosso et al. 2009; Cohen et al. 2011), and exciton transistors (High et al. 2007, 2008; Grosso et al. 2009). Exciton transport was also studied in potential energy gradients created by voltage gradients in electrodes (Hagn et al. 1995; Gärtner et al. 2006).

1.2 Transport Physics

Exciton transport is driven by drift and diffusion. Ivanov developed a drift-diffusion model that takes into account exciton heating and cooling, and quantum well disorder, see Ivanov et al. (2006) and Hammack et al. (2009). In steady-state, this drift-diffusion model is given by

$$\nabla\left[D_x\nabla n_x+\mu_x n_x\nabla\left(u_0 n_x+U_{\mathrm{QW}}+U_{\mathrm{external}}\right)\right]-n_x/\tau_{\mathrm{opt}}+\Lambda=0, \tag{1.1}$$

where n_x is the exciton density, D_x is the exciton diffusion constant, and μ_x is the exciton mobility. u_0 is the exciton–exciton repulsion. The exact value of u_0 depends on exciton correlations, however, throughout this work it is approximated using the parallel plate capacitor formula, $u_0 = 4\pi\left(e^2/\epsilon_b\right)d$, where ϵ_b is the dielectric coefficient for GaAs and d is the distance between quantum well centers. For the device geometry studied $u_0 \approx 1.6\,\mathrm{meV}/10^{10}$ excitons cm^{-2}. U_{QW} is the quantum well disorder, U_{external} is an externally applied potential, τ_{opt} is the optical recombination rate, and Λ is the exciton generation rate, determined by laser power. Quantum well disorder can be included in the diffusion coefficient using the thermionic model,

$$D=D_0\exp\left(-\frac{\left\langle U_{\mathrm{QW}}\right\rangle}{k_B T+u_0 n}\right) \tag{1.2}$$

This model accounts for excitons screening the quantum well disorder and exciton temperature. The diffusion coefficient and mobility are related by a generalization of the Einstein relationship $\mu = D_x/k_B T_0\left(\mathrm{e}^{T_0/T}-1\right) \approx D_x/k_B T$ for $T \gg T_0$, $T_0 = \left(\pi\hbar^2 n_x\right)/\left(2k_B M_x\right)$ is the exciton quantum degeneracy temperature with exciton mass in terms of the free electron mass, $M_x = 0.22m_e$. Laser heating is balanced by emission of acoustic phonons, described by

$$S_{\mathrm{phonon}}\left(T_0,T\right)=S_{\mathrm{pump}}\left(T_0,T,\Lambda,E_{\mathrm{inc}}\right). \tag{1.3}$$

This model describes all of the experiments in this dissertation, aside from the spin transport experiment. In order to describe spin transport, this model was generalized to include exciton spin. The details of this generalization are in Sects. 5.2–5.4.

1.3 Spin Physics

Due to conservation of angular momentum a circularly polarized laser excitation creates spin polarized excitons. An exciton is composed of a hole in the valence band $m_j = \pm 3/2$ and an electron in the conduction band $m_j = \pm 1/2$. This gives rise to four possible spin states, $m_j = \pm 1, \pm 2$, only $m_j = \pm 1$ are optically active due

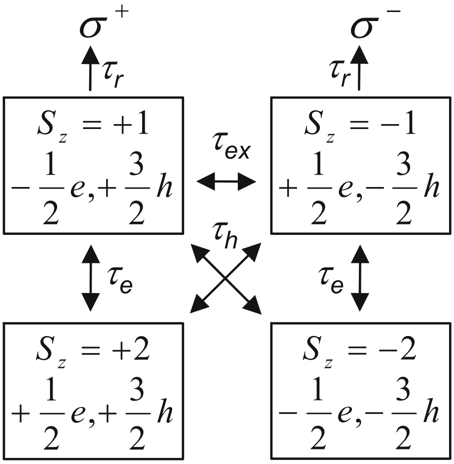

Fig. 1.4 Exciton spin flip pathways in GaAs. τ_r is the radiative recombination time, τ_e, (τ_h,) is the electron (hole) spin-flip time, τ_{ex} simultaneous electron-hole spin flip time. $\sigma^{\pm}$ indicates the polarization of emitted light

to conservation of angular momentum with the emitted photon. Figure 1.4 shows the possible spin-flip pathways in an exciton. An exciton can flip spin through an electron spin-flip, a hole spin-flip or a simultaneous electron and hole spin flip. Excitons undergo spin flip processes before optical decay, emitted light has the same polarization as the exciton. This allows the measurement of exciton spin by polarization resolved photoluminescence measurements. Optical methods have been used as a tool for precise injection, probe, and control of electron spin via photon polarization in semiconductors. A major role in the optical properties of semiconductors near the fundamental absorption edge is played by excitons. The spin dynamics of excitons in GaAs single quantum wells was extensively studied in the past, see Andreani and Bassani (1990), Maialle et al. (1993), Vinattieri et al. (1994) and the references therein. It was found that the spin relaxation time of excitons in single quantum wells is of the order of a few tens of picoseconds. Due to the short spin relaxation time, no spin transport of excitons was observed in single quantum wells. For the structures studied in this dissertation, the hole spin-flip time is fast compared to the electron spin-flip time (Uenoyama and Sham 1990; Maialle et al. 1993; Vinattieri et al. 1994).

In GaAs, there are two important mechanisms of exciton spin splitting, the Dresselhaus interaction and the electron–hole exchange interaction. Both of these mechanisms result in an energy difference between excitons of different spins. D'yakonov and Perel' quantified the effect of spin-splitting on spin relaxation. Qualitatively, the more excitons scatter, the longer their spin lifetime. This happens because each scattering event causes the exciton spin to precess about a different arbitrary axis. If excitons scatter frequently, the exciton does not precess much before scattering again. In this case, the average exciton spin is mostly unchanged. In contrast, if the exciton precesses before scattering, the exciton spin will be oriented in a random direction, and the average exciton spin tends to zero (D'yakonov and Perel' 1971c).

1.3.1 D'yakanov and Perel' Spin Relaxation

For hamiltonians of the form

$$H = \frac{p^2}{2m} + \frac{\hbar}{2}\left(\vec{\sigma} \cdot \vec{\Omega}\left(\vec{p}\right)\right) \tag{1.4}$$

where $\vec{p}$ is the electron momentum, $\vec{\sigma}$ is the electron spin, $\vec{\Omega}$ is the spin precession frequency, and m is the electron mass. The spin relaxation time is given by

$$\tau_s^{-1} = \left\langle \Omega^2 \tau \right\rangle \tag{1.5}$$

where τ is the momentum relaxation time given by

$$\mu = \frac{e\tau}{m}. \tag{1.6}$$

μ, e, and m are the electron mobility, charge, and mass respectively (D'yakonov and Perel' 1971c).

1.3.2 Dresselhaus Interaction

The Dresselhaus interaction arises from spatial inversion asymmetry. GaAs is made up of two face-centered sublattices. Since each sublattice is made from a different element, spatial inversion changes the lattice structure. This allows terms in the Hamiltonian of the form p^3 to be non-zero. The Dresselhaus interaction arises as a third order perturbation on the GaAs band structure, one of the band mixing terms contains spin orbit coupling (Winkler 2003). The Hamiltonian is given by

$$H = \frac{p^2}{2m} + \frac{\hbar}{2}\left(\vec{\sigma} \cdot \vec{\Omega}\right) \tag{1.7}$$

where

$$\vec{\Omega} = \gamma_c \vec{\kappa}, \tag{1.8}$$

where $\gamma_c \approx 27.5\,\mathrm{eV}\,\text{Å}^3$ in the case of GaAs. For bulk materials $\vec{\kappa}$ is given by

$$\kappa_x = p_x\left(p_y^2 - p_z^2\right) \tag{1.9}$$

with κ_y and κ_z given by cyclic permutation.

D'yakonov and Kachorovskiĭ specialized the Dresselhaus interaction for the case of a quantum well. In a quantum well, q is the momentum along the confinement direction. For a quantum well, $\langle q \rangle = 0$ and $\langle q^2 \rangle \neq 0$ is determined by the width of the quantum well and barrier height. In the approximation $\langle q^2 \rangle \gg k^2_{\text{thermal}}$, the Dresselhaus interaction reduces to first order in k_{thermal}. In particular, the momentum dependence reduces to

$$\langle \kappa_x \rangle = \langle q^2 \rangle \left[2n_x \left(n_y k_y - n_z k_z \right) + \left(n_y^2 - n_z^2 \right) k_z \right] \tag{1.10}$$

where $\vec{n}$ is the growth direction and $\vec{k}$ is the in-plane thermal momentum (D'yakonov and Kachorovskiĭ (1986)).

Using this model, the spin splitting constant, $\langle q^2 \rangle \gamma_c$, can be measured experimentally and independently estimated from the geometry of the quantum wells. This measurement is discussed in Chap. 5.

1.3.3 Electron–Hole Exchange Interaction

The exchange interaction takes place between the electron and hole in an exciton, spin relaxation follows the D'yakonov and Perel' model. Spin relaxation due to the electron–hole exchange interaction is designated by τ_{ex}. In a single quantum well, the electron–hole exchange interaction is an important part of spin relaxation (Maialle et al. 1993; Vinattieri et al. 1994). $\tau_{\text{ex}} \propto \tau_{\text{r}}^2$, so for the coupled quantum wells studied in this dissertation, τ_{ex} is suppressed by six orders of magnitude compared to a single quantum well. This estimate is discussed in Chap. 5.

1.4 Experimental Methods

For the devices (Chaps. 2–4), the CQW structure is grown by molecular beam epitaxy. An n^+-GaAs layer with $n_{\text{Si}} = 10^{18}\,\text{cm}^3$ serves as a homogeneous bottom electrode. A semitransparent top electrode is fabricated by depositing a 100 nm indium tin oxide layer. Two 8 nm GaAs QWs separated by a 4 nm $\text{Al}_{0.33}\text{Ga}_{0.67}\text{As}$ barrier are positioned 100 nm above the n^+-GaAs layer within an undoped 1 μm thick $\text{Al}_{0.33}\text{Ga}_{0.67}\text{As}$ layer. Positioning the CQW closer to the homogeneous electrode suppresses the in-plane electric field (Hammack et al. 2006), which otherwise can lead to exciton dissociation (Zimmermann et al. 1997).

For the measurement of spin transport (Chap. 5) there were no shaped electrodes, so exciton dissociation was not a concern and the QWs were grown in the center of the structure. See Chap. 5 for details.

1.5 Dissertation Overview

I studied controlled exciton transport using three different systems, a ramp, a crossed-ramp transistor, and a conveyer.

The ramp is conceptually similar to an electric field. Excitons are neutral particles so simply applying an electric field in the direction of transport will not affect the exciton. Instead, by manipulating the electric field perpendicular to the direction of exciton motion a linear potential gradient is created that applies a constant force to excitons similar to the way an electric field applies a constant force to electrons. Details about controlling exciton transport via ramps are given in Chap. 2.

The crossed-ramp builds on the ramp experiment, it consists of two ramps oriented perpendicular to each other. This device is an optically controlled exciton transistor. Details about controlling exciton transport via a crossed-ramp transistor are given in Chap. 3.

The conveyer experiment uses a moving sinusoidal potential to transport excitons, conceptually similar to a CCD. The moving sinusoidal potential is created by a set of seven independently addressable electrodes driven by phase shifted sinewaves. The conveyer offers a wide degree of flexibility, it is simple to control the speed and strength of the conveyer using a signal generator. Details about controlling exciton transport via conveyer are given in Chap. 4.

These three experiments cover different methods of controlling exciton transport. In addition to these experiments, I studied exciton spin transport. I observed spatially indirect excitons transport spin, over substantial distances, up to several micrometers. This was achieved due to orders of magnitude enhancement of the exciton spin relaxation time of indirect excitons with respect to excitons in single quantum wells. This experiment is described in Chap. 5.

References

M. Alloing, A. Lemaître, F. Dubin, Quantum signature blurred by disorder in indirect exciton gases. Europhys. Lett. **93**(1), 17007 (2011)

M. Alloing, A. Lemaître, E. Galopin, F. Dubin, Non-linear dynamics and inner-ring photoluminescence pattern of indirect excitons. e-print arXiv:1202.1985 (2012)

A. Amo, T.C.H. Liew, C. Adrados, R. Houdré, E. Giacobino, A.V. Kavokin, A. Bramati, Exciton–polariton spin switches. Nat. Photon. **4**, 361–366 (2010)

L.C. Andreani, F. Bassani, Exchange interaction and polariton effects in quantum-well excitons. Phys. Rev. B **41**(11), 7536–7544 (1990)

L.C. Andreani, F. Tassone, F. Bassani, Radiative lifetime of free excitons in quantum wells. Solid State Commun. **77**(9), 641–645 (1991)

I. Appelbaum, B. Huang, D.J. Monsma, Electronic measurement and control of spin transport in silicon. Nature **447**, 295–298 (2007)

A.G. Aronov, G.E. Pikus, Spin injection into semiconductros. Sov. Phys. Semicond. **10**, 698 (1976)

D.D. Awschalom, M.E. Flatté, Challenges for semiconductor spintronics. Nat. Phys. **3**, 153–159 (2007)

M. Baldo, V. Stojanović, Optical switching: excitonic interconnects. Nat. Photon. **3**, 558–560 (2009)

D. Ballarini, M. De Giorgi, E. Cancellieri, R. Houdré, E. Giacobino, R. Cingolani, A. Bramati, G. Gigli, D. Sanvitto, All-optical polariton transistor. Nat. Commun. **4**, 1778 (2013)

L.V. Butov, A.I. Filin, Anomalous transport and luminescence of indirect excitons in AlAs/GaAs coupled quantum wells as evidence for exciton condensation. Phys. Rev. B **58**(4), 1980–2000 (1998)

L.V. Butov, A. Imamoglu, A.V. Mintsev, K.L. Campman, A.C. Gossard, Photoluminescence kinetics of indirect excitons in GaAs/Al$_x$Ga$_{1-x}$As coupled quantum wells. Phys. Rev. B **59**(3), 1625 (1999)

L.V. Butov, A.C. Gossard, D.S. Chemla, Macroscopically ordered state in an exciton system. Nature **418**, 751–754 (2002)

S.G. Carter, Z. Chen, S.T. Cundiff, Optical measurement and control of spin diffusion in n-doped GaAs quantum wells. Phys. Rev. Lett. **97**(13), 136602 (2006)

K. Cohen, R. Rapaport, P.V. Santos, Remote dipolar interactions for objective density calibration and flow control of excitonic fluids. Phys. Rev. Lett. **106**, 126402 (2011)

I. D'Amico, G. Vignale, Spin diffusion in doped semiconductors: the role of Coulomb interactions. Europhys. Lett. **55**(4), 566 (2001)

B. Deveaud, F. Clerot, N. Roy, K. Satzke, B. Sermage, D.S. Katzer, Enhanced radiative recombination of free excitons in GaAs quantum wells. Phys. Rev. Lett. **67**(17), 2355–2358 (1991)

M.I. D'yakonov, V.Yu. Kachorovskiĭ, Spin relaxation of two-dimensional electrons in noncentrosymmetric semiconductors. Sov. Phys. Semicond. **20**, 110 (1986)

M.I. D'yakonov, V.I. Perel', Current-induced spin orientation of electrons in semiconductors. Phys. Lett. A **35**(6), 459–460 (1971a)

M.I. D'yakonov, V.I. Perel', Possibility of orienting electron spins with current. Sov. Phys. JETP Lett. **13**(11), 467 (1971b)

M.I. D'yakonov, V.I. Perel', Spin orientation of electrons associated with the interband absorption of light in semiconductors. Sov. Phys. JETP **33**, 1053–1059 (1971c)

R.I. Dzhioev, B.P. Zakharchenya, V.L. Korenev, M.N. Stepanova, Spin diffusion of optically oriented electrons and photon entrainment in n-gallium arsenide. Fiz. Tverd. Tela **39**, 1975–1979 (1997)

J. Feldmann, G. Peter, E.O. Göbel, P. Dawson, K. Moore, C. Foxon, R.J. Elliott, Linewidth dependence of radiative exciton lifetimes in quantum wells. Phys. Rev. Lett. **59**(20), 2337–2340 (1987)

T. Gao, P.S. Eldridge, T.C.H. Liew, S.I. Tsintzos, G. Stavrinidis, G. Deligeorgis, Z. Hatzopoulos, P.G. Savvidis, Polariton condensate transistor switch. Phys. Rev. B **85**, 235102 (2012)

A. Gärtner, A.W. Holleitner, J.P. Kotthaus, D. Schuh, Drift mobility of long-living excitons in coupled GaAs quantum wells. Appl. Phys. Lett. **89**(5), 052108 (2006)

G. Grosso, J. Graves, A.T. Hammack, A.A. High, L.V. Butov, M. Hanson, A.C. Gossard, Excitonic switches operating at around 100 K. Nat. Photon. **3**, 577–580 (2009)

M. Hagn, A. Zrenner, G. Böhm, G. Weimann, Electric-field-induced exciton transport in coupled quantum well structures. Appl. Phys. Lett. **67**(2), 232–234 (1995)

A.T. Hammack, N.A. Gippius, S. Yang, G.O. Andreev, L.V. Butov, M. Hanson, A.C. Gossard, Excitons in electrostatic traps. J. Appl. Phys. **99**(6), 066104 (2006)

A.T. Hammack, L.V. Butov, J. Wilkes, L. Mouchliadis, E.A. Muljarov, A.L. Ivanov, A.C. Gossard, Kinetics of the inner ring in the exciton emission pattern in coupled GaAs quantum wells. Phys. Rev. B **80**(15), 155331 (2009)

A.A. High, A.T. Hammack, L.V. Butov, M. Hanson, A.C. Gossard, Exciton optoelectronic transistor. Opt. Lett. **32**(17), 2466–2468 (2007)

A.A. High, E.E. Novitskaya, L.V. Butov, M. Hanson, A.C. Gossard, Control of exciton fluxes in an excitonic integrated circuit. Science **321**(5886), 229–231 (2008)

A.A. High, A.K. Thomas, G. Grosso, M. Remeika, A.T. Hammack, A.D. Meyertholen, M.M. Fogler, L.V. Butov, M. Hanson, A.C. Gossard, Trapping indirect excitons in a GaAs quantum-well structure with a diamond-shaped electrostatic trap. Phys. Rev. Lett. **103**(8), 087403 (2009)

J.E. Hirsch, Spin hall effect. Phys. Rev. Lett. **83**(9), 1834–1837 (1999)

A.L. Ivanov, L.E. Smallwood, A.T. Hammack, S. Yang, L.V. Butov, A.C. Gossard, Origin of the inner ring in photoluminescence patterns of quantum well excitons. Europhys. Lett. **73**(6), 920–926 (2006)

J.M. Kikkawa, D.D. Awschalom, Lateral drag of spin coherence in gallium arsenide. Nature **397**, 139–141 (1999)

C. Kittel, *Introduction to Solid State Physics*, 8th edn. (Wiley, Hoboken, NJ, 2005)

Y.Y. Kuznetsova, M. Remeika, A.A. High, A.T. Hammack, L.V. Butov, M. Hanson, A.C. Gossard, All-optical excitonic transistor. Opt. Lett. **35**(10), 1587–1589 (2010)

A.V. Larionov, V.B. Timofeev, J. Hvam, K. Soerensen, Interwell excitons in GaAs/AlGaAs double quantum wells and their collective properties. Sov. Phys. JETP **90**(6), 1093–1104 (2000)

J.R. Leonard, S. Yang, L.V. Butov, A.C. Gossard, Spin transport of indirect excitons in GaAs coupled quantum wells (2008). arXiv:0808.2402v3

J.R. Leonard, M. Remeika, M.K. Chu, Y.Y. Kuznetsova, A.A. High, L.V. Butov, J. Wilkes, M. Hanson, A.C. Gossard, Transport of indirect excitons in a potential energy gradient. Appl. Phys. Lett. **100**(23), 231106 (2012)

M.Z. Maialle, E.A. de Andrada e Silva, L.J. Sham, Exciton spin dynamics in quantum wells. Phys. Rev. Lett. **47**(23), 15776–15788 (1993)

D.A.B. Miller, D.S. Chemla, T.C. Damen, A.C. Gossard, W. Wiegmann, T.H. Wood, C.A. Burrus, Electric field dependence of optical absorption near the band gap of quantum-well structures. Phys. Rev. B **32**(2), 1043–1060 (1985)

H.S. Nguyen, D. Vishnevsky, C. Sturm, D. Tanese, D. Solnyshkov, E. Galopin, A. Lemaître, I. Sagnes, A. Amo, G. Malpuech, J. Bloch, Realization of a double-barrier resonant tunneling diode for cavity polaritons. Phys. Rev. Lett. **110**, 236601 (2013)

M. Remeika, J.C. Graves, A.T. Hammack, A.D. Meyertholen, M.M. Fogler, L.V. Butov, M. Hanson, A.C. Gossard, Localization-delocalization transition of indirect excitons in lateral electrostatic lattices. Phys. Rev. Lett. **102**(18), 186803 (2009)

M. Remeika, M.M. Fogler, L.V. Butov, M. Hanson, A.C. Gossard, Two-dimensional electrostatic lattices for indirect excitons. Appl. Phys. Lett. **100**(6), 061103 (2012)

G.J. Schinner, E. Schubert, M.P. Stallhofer, J.P. Kotthaus, D. Schuh, A.K. Rai, D. Reuter, A.D. Wieck, A.O. Govorov, Electrostatically trapping indirect excitons in coupled $\mathrm{In}_x\mathrm{Ga}_{1-x}\mathrm{As}$ quantum wells. Phys. Rev. B **83**, 165308 (2011)

V. Sih, R.C. Myers, Y.K. Kato, W.H. Lau, A.C. Gossard, D.D. Awschalom, Spatial imaging of the spin Hall effect and current-induced polarization in two-dimensional electron gases. Nat. Phys. **1**, 31–35 (2005)

C. Sturm, D. Tanese, H.S. Nguyen, H. Flayac, E. Galopin, A. Lemaître, I. Sagnes, D. Solnyshkov, A. Amo, G. Malpuech, J. Bloch, All-optical phase modulation in a cavity-polariton Mach-Zehnder interferometer. Nat. Commun. **5**, 3278 (2014)

T. Uenoyama, L.J. Sham, Carrier relaxation and luminescence polarization in quantum wells. Phys. Rev. B **42**(11), 7114 (1990)

L. Viña, Spin relaxation in low-dimensional systems. J. Phys. Condens. Matter **11**, 5929–5952 (1999)

A. Vinattieri, J. Shah, T.C. Damen, D.S. Kim, L.N. Pfeiffer, M.Z. Maialle, L.J. Sham, Exciton dynamics in GaAs quantum wells under resonant excitation. Phys. Rev. B **50**(15), 10868–10879 (1994)

X.P. Vögele, D. Schuh, W. Wegscheider, J.P. Kotthaus, A.W. Holleitner, Density enhanced diffusion of dipolar excitons within a one-dimensional channel. Phys. Rev. Lett. **103**(12), 126402 (2009)

Z. Vörös, R. Balili, D.W. Snoke, L. Pfeiffer, K. West, Long-distance diffusion of excitons in double quantum well structures. Phys. Rev. Lett. **94**(22), 226401 (2005)

C.P. Weber, N. Gedik, J.E. Moore, J. Orenstein, J. Stephens, D.D. Awschalom, Observation of spin Coulomb drag in a two-dimensional electron gas. Nature **437**, 1330–1333 (2005)

A.G. Winbow, J.R. Leonard, M. Remeika, Y.Y. Kuznetsova, A.A. High, A.T. Hammack, L.V. Butov, J. Wilkes, A.A. Guenther, A.L. Ivanov, M. Hanson, A.C. Gossard, Electrostatic conveyer for excitons. Phys. Rev. Lett. **106**(19), 196806 (2011)

R. Winkler, *Spin–Orbit Coupling Effects in Two-Dimensional Electron and Hole Systems* (Springer, Berlin/Heidelberg/New York, 2003)

I.A. Young, E. Mohammed, J.T.S. Liao, A.M. Kern, S. Palermo, B.A. Block, M.R. Reshotko, P.L.D. Chang, Optical I/O technology for tera-scale computing. IEEE J. Solid State Circuits **45**, 235 (2010)

P.Y. Yu, M. Cardona, *Fundamentals of Semiconductors*, 4th edn. (Springer, Heidelberg/Dordrecht/London/New York, 2005)

S. Zimmermann, A.O. Govorov, W. Hansen, J.P. Kotthaus, M. Bichler, W. Wegscheider, Lateral superlattices as voltage-controlled traps for excitons. Phys. Rev. B **56**(20), 13414–13421 (1997)

Chapter 2
Controlled Exciton Transport via a Ramp

2.1 Introduction

In this chapter, we study exciton transport in a potential energy gradient—a ramp—created by a shaped electrode at constant voltage. We utilize the ability to control exciton energy by electrode shape (Kuznetsova et al. 2010) and design the shape of a top electrode on the sample surface so that a voltage applied to it creates a constant potential energy gradient for indirect excitons in the CQW. The excitonic ramp realizes directed transport of excitons as a diode realizes directed transport of electrons.

The advantages of this shaped-electrode-method include the suppression of heating by electric currents in electrodes (such currents may appear in the case when the ramp potential is created by a voltage gradient in the top electrode) and the opportunity to engineer the exciton energy profile along the ramp by designing the electrode shape. We also measure exciton transport in a narrow channel formed by a voltage applied to an electrode stripe of constant width—a flat-energy channel (Grosso et al. 2009; Cohen et al. 2011).

2.2 Ramp Design

The principle of the ramp is the following: a thinner electrode produces a smaller electric field, F_z in the QWs due to field divergence near the electrode edges, therefore narrowing the electrode increases the exciton energy thus creating a ramp potential for excitons. We want to design an electrode to obtain a linear ramp with a constant gradient of the exciton energy. The energy gradient for indirect excitons in the ramp can be controlled by the length of the ramp and voltage—it is proportional to V_e.

J. Leonard, *Exciton Transport Phenomena in GaAs Coupled Quantum Wells*,
Springer Theses, https://doi.org/10.1007/978-3-319-69733-8_2

We used electrode shape to control exciton energy (Kuznetsova et al. 2010). The geometry of the quantum wells (Fig. 2.1a) and geometry of the sample (Fig. 2.1b) determine the conversion between electric field and indirect exciton energy shift. We perform simulations to calculate electric field at the CQW location (Fig. 2.1b) and convert the electric field to indirect exciton potential. In this instance the conversion constant is $\approx$ 10 meV/(10^6 V/m). The geometry of the ramp leads to a simple design. Physical considerations suggest the narrowest portion of the ramp be 1 μm wide and the widest portion 3 μm wide. The narrow width is chosen based on practical optical alignment considerations and the widest portion is chosen based on decreasing electric fringe fields beyond that width. The length of the ramp is 10 μm, long enough to see transport along the ramp on both sides of the laser spot, but short to maximize the potential gradient. We started by simulating a 20 μm triangular ramp containing a portion that was 10 μm long, 1 μm wide at the start and 3 μm at the end, Fig. 2.1c. We took the indirect exciton energy shift from this simulation (Fig. 2.1d) and inverted it to have ramp width as a function of energy shift. We then interpolated with a linear potential (Fig. 2.1e) giving us the ideal ramp width (Fig. 2.1f). The shape of this ramp was re-simulated to confirm accuracy. This method works for various length ramps provided the 1 μm and 3 μm region are spaced according to the final ramp length. Figure 2.2a is an SEM image of the final ramp.

2.3 Experimental Methods

The CQW structure is described in Sect. 1.4. Excitons are photoexcited by a 633 nm HeNe laser focused to a spot with full width half maximum 4 μm.

2.4 Qualitative Results

Figure 2.2b shows the profile of the indirect exciton photoluminescence (PL) intensity $I(x)$ in the 3 μm channel. The laser excitation profile is shown in gray. The emission pattern has two maxima around the excitation spot and is nearly symmetric relative to the excitation spot position. This pattern is similar to the inner ring studied previously (Butov et al. 2002; Ivanov et al. 2006, 2010; Hammack et al. 2009; Alloing et al. 2012; Stern et al. 2008). The inner ring was explained in terms of exciton transport and cooling: optical excitation heats the exciton gas, excitons cool towards the lattice temperature as they travel away from the excitation spot, the cooling results in an increase in the occupation of the low-energy optically active exciton states and, as a result, the appearance of an emission ring around the excitation spot (Butov et al. 2002; Ivanov et al. 2006, 2010; Hammack et al. 2009; Alloing et al. 2012).

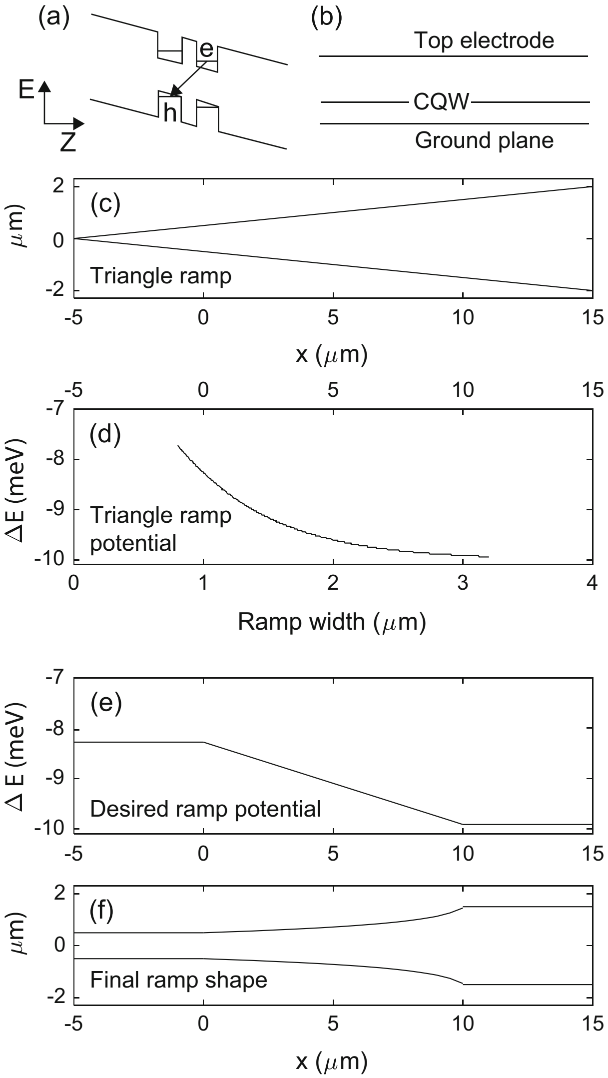

Fig. 2.1 Ramp design. (**a**) CQW band diagram. e, electron; h, hole. (**b**) QW sample schematic. We want to design a top electrode to create a specific electric field in the CQW layer. (**c**) Top electrode initial design, the electrode covers the area inside the triangle. (**d**) Simulated indirect exciton energy shift for top electrode (**c**), $V_e = -1\text{V}$. (**e**) Desired indirect exciton energy shift. (**f**) Top electrode shape that creates the exciton potential in (**e**), the electrode covers the region inside the shape. Designed by transposing the potential in (**d**) to get electrode width as a function of energy shift, and interpolating with the desired energy shift

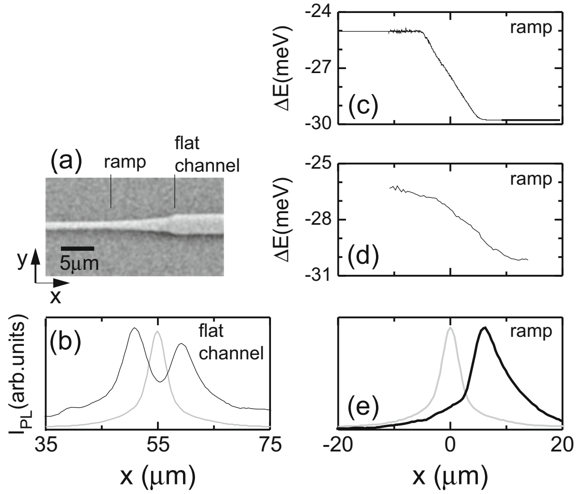

Fig. 2.2 Ramp overview and operation. (**a**) Scanning electron microscope image of the electrode, which forms the linear potential energy gradient—ramp (center) and flat-energy channels (sides) for indirect excitons. (**b**) Indirect exciton PL profile in the flat channel (black). $P_{\text{ex}} = 0.5\,\mu\text{W}$, $T_{\text{bath}} = 1.6\,\text{K}$. Laser excitation profile is shown in gray. (**c**) Simulated potential energy for indirect excitons in the ramp surrounded by flat-energy channels (thin lines show extrapolations). (**d**) Indirect exciton PL energy in the ramp. $P_{\text{ex}} = 0.02\,\mu\text{W}$, $T_{\text{bath}} = 5.4\,\text{K}$. (**e**) Indirect exciton PL profile in the ramp (black). $P_{\text{ex}} = 0.5\,\mu\text{W}$, $T_{\text{bath}} = 1.6\,\text{K}$. Laser excitation profile is shown in gray. $V_e = -3\,\text{V}$ for all data

Figure 2.2c presents a theoretical numerical simulation of the potential energy profile for indirect excitons edF_z for constant voltage $V_e = -3\,\text{V}$ applied to the top electrode shown in Fig. 2.2a. The ramp is surrounded by flat-energy channels where the electrode width is constant (1 μm left of the ramp and 3 μm right of the ramp). The energy of indirect excitons is constant in the flat-energy channels (Fig. 2.2c). Figure 2.2d shows the measured spatial profile of the emission energy of indirect excitons along the ramp $E(x) = \int EI(x, E)dE/I(x)$, where $I(x) = \int I(x, E)dE$. The measurement was performed at $T_{\text{bath}} = 5.4\,\text{K}$ and $P_{\text{ex}} = 0.02\,\mu\text{W}$: a higher temperature was chosen to reduce the effect of QW disorder and a low laser excitation—to reduce the effect of exciton–exciton repulsion, these effects are described below. The energy of the indirect excitons was measured relative to the direct exciton energy, which is practically independent of x. The measured (Fig. 2.2d) and calculated (Fig. 2.2c) ramp profiles are qualitatively similar (note that the measured energy difference between the direct and indirect excitons also includes the difference between the direct and indirect exciton binding energies, a few meV for the CQW (Butov et al. 1999)).

Figure 2.2e shows the profile of the indirect exciton PL intensity $I(x)$ in the ramp. The laser excitation profile is shown in gray. In contrast to the flat-energy channel (Fig. 2.2b), on the ramp (Fig. 2.2e), $I(x)$ is asymmetric relative to the excitation spot due to exciton transport along the potential energy gradient.

2.5 Quantitative Results

We studied exciton transport in the ramp for different excitation powers P_{ex} and cryostat temperatures T_{bath}. Exciton transport in the ramp is presented by the extension of the exciton cloud along the energy gradient (Fig. 2.3). We quantify it by the first moment of the PL intensity $M_1 = \int xI(x)dx / \int I(x)dx$, which characterizes the average transport distance of indirect excitons along the ramp. Figure 2.3 shows that the exciton transport distance along the ramp increases with density. We attribute this to the screening of the disorder in the structure by indirect excitons. The screening originates from the repulsive interaction between indirect excitons, which are dipoles oriented perpendicular to the QW plane (Ivanov 2002; Ivanov et al. 2010). Such screening improves exciton mobility and, as a result, increases their transport distance along the energy gradient. Figure 2.3 also shows that exciton transport distance along the ramp increases with temperature. We attribute this to the thermal activation of indirect excitons in the disorder potential that facilitates their transport. These interpretations are in agreement with the theoretical numerical model presented in Sect. 2.6. A drop of M_1 observed at the highest excitation powers can be related to a photoexcitation-induced reduction of the electric field F_z in the device.

The measurements of exciton transport in a ramp and in a flat-energy region allow estimating the exciton temperature T. The former measurement provides an estimate for the exciton mobility μ_x, the latter—for the exciton diffusion coefficient D_x, and the Einstein relationship between them—for the exciton temperature. The

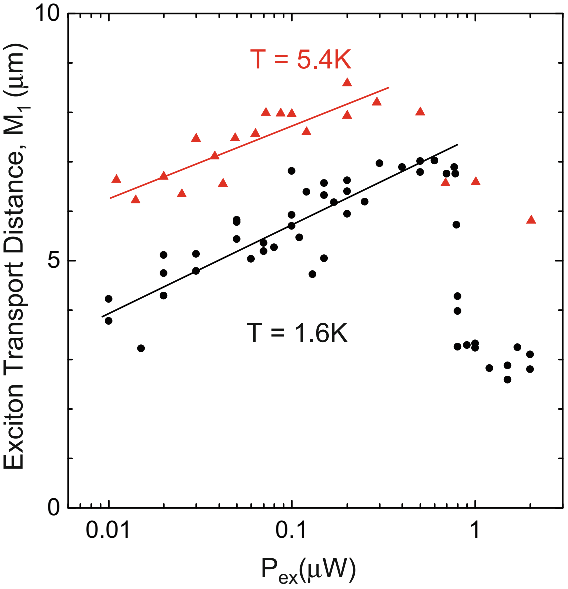

Fig. 2.3 Observed ramp transport distance dependence on exciton density and sample temperature. The average transport distance of indirect excitons along the ramp M_1 as a function of excitation density P_{ex} for $T_{\mathrm{bath}} = 1.6\,\mathrm{K}$ (black circles) and 5.4 K (red triangles), $V_e = -3\,\mathrm{V}$

exciton diffusion coefficient can be estimated using $D_x \approx w^2/\tau_{\text{opt}}$, where w is the half-width at half-maximum of the indirect exciton emission cloud in the flat-energy region and τ_{opt} is the indirect exciton lifetime ($\tau_{\text{opt}} \approx 50\,\text{ns}$ in the structure). The exciton mobility can be estimated using $\mu_x = -\frac{M_1}{\tau_{\text{opt}}\nabla U_{\text{ramp}}}$, where ∇U_{ramp} is the exciton potential energy gradient in the ramp. For $T_{\text{bath}} = 1.6\,\text{K}$ and $P_{\text{ex}} = 0.02\,\mu\text{W}$, the estimate gives $D_x \sim 3\,\text{cm}^2/\text{s}$, $\mu_x \sim 3000\,\text{cm}^2/\text{eVs}$, and $T = \frac{D_x}{k_B \mu_x} \sim 10\,\text{K}$ (k_B is the Boltzmann constant). This estimate is consistent with the exciton temperature in the excitation spot obtained within the theoretical model for the exciton energy relaxation and transport in a ramp (Fig. 2.4a). This model is described in Sect. 2.6.

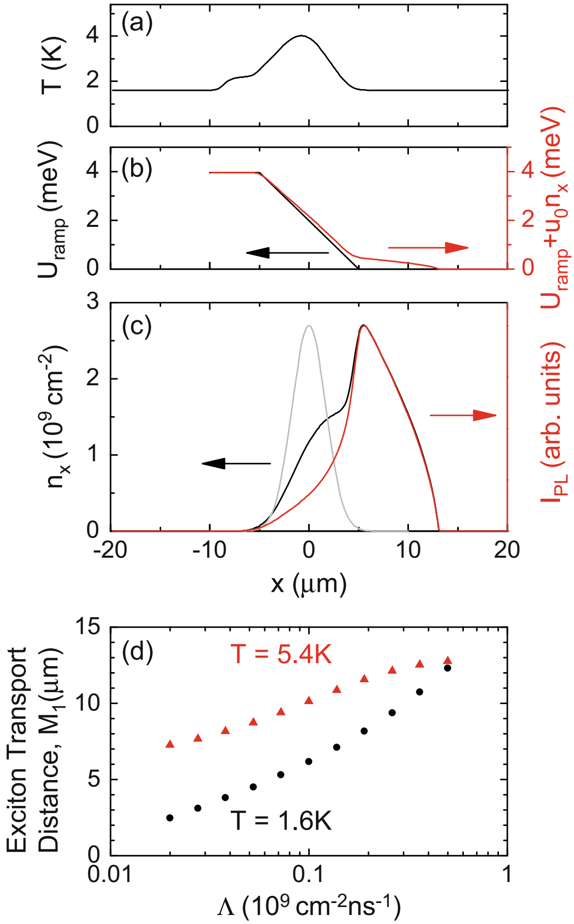

Fig. 2.4 Theoretical ramp transport distance dependence on exciton density and sample temperature. (**a**) Exciton temperature. (**b**) Bare ramp potential U_{ramp} and screened ramp potential $U_{\text{ramp}} + u_0 n_x$. (**c**) Exciton density (black) and PL intensity (red). Laser excitation profile is shown in gray. $\Lambda = 10^8\,\text{cm}^{-2}\,\text{ns}^{-1}$, $T_{\text{bath}} = 1.6\,\text{K}$. (**d**) The average transport distance of indirect excitons along the ramp M_1 as a function of exciton generation rate Λ for $T_{\text{bath}} = 1.6$ (black) and 5.4 K (red)

2.6 Theoretical Model

We modeled the in-plane transport of excitons in the ramp using the nonlinear partial differential equation for exciton density n_x outlined in Sect. 1.2 modified to include the ramp potential:

$$\nabla\left[D_x\nabla n_x+\mu_x n_x\nabla\left(u_0 n_x+U_{\mathrm{ramp}}\right)\right]-n_x/\tau_{\mathrm{opt}}+\Lambda=0. \tag{2.1}$$

The first and second terms in the square brackets account for exciton diffusion and drift, respectively. In the one-dimensional geometry relevant to the experiment, $\nabla=\partial/\partial x$. The exciton dipole–dipole repulsion, which is approximated by $u_0 n_x$ with $u_0=4\pi de^2/\varepsilon_b$ (ε_b is the background dielectric constant), (Ivanov 2002; Ivanov et al. 2006, 2010) and the ramp potential $U_{\mathrm{ramp}}=edF_z$ are included in the drift term. The decay rate of excitons is given by $1/\tau_{\mathrm{opt}}$. $\Lambda(x)$ is the exciton generation rate. The diffusion coefficient and mobility are related by the generalized Einstein relationship $\mu_x=D_x/k_BT_0\left(e^{T_0/T}-1\right)$, where $T_0=\left(2\pi\hbar^2 n_x\right)/\left(M_x g k_B\right)$ is the quantum degeneracy temperature. Here, $g=4$ is the spin degeneracy. The diffusion coefficient is given by the thermionic model $D_x=D_0 e^{-U_0/(u_0 n_x+k_BT)}$, where $U_0/2=0.75\,\mathrm{meV}$ is the amplitude of disorder potential in the structure (Ivanov 2002). In addition, we included a thermalization equation to account for energy relaxation of photoexcited excitons:

$$S_{\mathrm{phonon}}\left(T_0,T\right)=S_{\mathrm{pump}}\left(T_0,T,\Lambda,E_{\mathrm{inc}}\right), \tag{2.2}$$

where S_{phonon} is the cooling rate due to bulk longitudinal acoustic phonon emission, S_{pump} is the heating rate due to the laser excitation, and E_{inc} is the excess energy of photoexcited excitons (17 meV in the simulations). Expressions for S_{phonon}, S_{pump}, τ_{opt} and all other parameters of the model are given in Ivanov (2002), Ivanov et al. (2006), Hammack et al. (2009).

The results of the simulations are presented in Fig. 2.4. The calculated exciton temperature in the excitation spot (Fig. 2.4a) is close to the temperature estimate above. Figure 2.4b shows the bare ramp potential U_{ramp} and the ramp potential screened by the exciton–exciton repulsion $U_{\mathrm{ramp}}+u_0 n_x$. Figure 2.4c shows the density and PL intensity of indirect excitons. The latter is qualitatively similar to the measured PL intensity (Fig. 2.2e). Figure 2.4d shows the average transport distance of indirect excitons along the ramp M_1 as a function of exciton generation rate $\Lambda(x)$. Within the model, the exciton transport distance along the ramp increases with density due to the screening of the disorder in the structure by repulsively interacting indirect excitons and increases with temperature due to the thermal activation of indirect excitons in the disorder potential. These features observed in the model are qualitatively similar to the experimental data, compare Figs. 2.3 and 2.4d.

2.7 Summary

We report on the realization of an electrostatic ramp potential for indirect excitons using a shaped electrode at constant voltage and on experimental and theoretical studies of exciton transport along the ramp.

2.8 Further Reading

For a ramp of constant width, but variable electrode density, see Dorow et al. (2016).

References

M. Alloing, A. Lemaître, E. Galopin, F. Dubin, Non-linear dynamics and inner-ring photoluminescence pattern of indirect excitons (2012). e-print arXiv:1202.1985

L.V. Butov, A.A. Shashkin, V.T. Dolgopolov, K.L. Campman, A.C. Gossard, Magneto-optics of the spatially separated electron and hole layers in GaAs/$Al_xGa_{1-x}As$ coupled quantum wells. Phys. Rev. B **60**(12), 8753–8758 (1999)

L.V. Butov, A.C. Gossard, D.S. Chemla, Macroscopically ordered state in an exciton system. Nature **418**, 751–754 (2002)

K. Cohen, R. Rapaport, P.V. Santos, Remote dipolar interactions for objective density calibration and flow control of excitonic fluids. Phys. Rev. Lett. **106**, 126402 (2011)

C.J. Dorow, Y.Y. Kuznetsova, J.R. Leonard, M.K. Chu, L.V. Butov, J. Wilkes, M. Hanson, A.C. Gossard, Indirect excitons in a potential energy landscape created by a perforated electrode. Appl. Phys. Lett. **108**, 073502 (2016)

G. Grosso, J. Graves, A.T. Hammack, A.A. High, L.V. Butov, M. Hanson, A.C. Gossard, Excitonic switches operating at around 100 K. Nat. Photon. **3**, 577–580 (2009)

A.T. Hammack, L.V. Butov, J. Wilkes, L. Mouchliadis, E.A. Muljarov, A.L. Ivanov, A.C. Gossard, Kinetics of the inner ring in the exciton emission pattern in coupled GaAs quantum wells. Phys. Rev. B **80**(15), 155331 (2009)

A.L. Ivanov, Quantum diffusion of dipole-oriented indirect excitons in coupled quantum wells. Europhys. Lett. **59**(4), 586–591 (2002)

A.L. Ivanov, L.E. Smallwood, A.T. Hammack, S. Yang, L.V. Butov, A.C. Gossard, Origin of the inner ring in photoluminescence patterns of quantum well excitons. Europhys. Lett. **73**(6), 920–926 (2006)

A.L. Ivanov, E.A. Muljarov, L. Mouchliadis, R. Zimmermann, Comment on "Photoluminescence ring formation in coupled quantum wells: excitonic versus ambipolar diffusion". Phys. Rev. Lett. **104**(17), 179701 (2010)

Y.Y. Kuznetsova, A.A. High, L.V. Butov, Control of excitons by laterally modulated electrode density. Appl. Phys. Lett. **97**(20), 201106 (2010)

M. Stern, V. Garmider, E. Segre, M. Rappaport, V. Umansky, Y. Levinson, I. Bar-Joseph, Photoluminescence ring formation in coupled quantum wells: excitonic versus ambipolar diffusion. Phys. Rev. Lett. **101**(25), 257402 (2008)

Chapter 3
Controlled Exciton Transport via an Optically Controlled Exciton Transistor

3.1 Introduction

There is interest in developing optical devices due to potential advantages over electronic devices for chip to chip communication (Young et al. 2010; High et al. 2008; Baldo and Stojanović 2009) additionally, the increase in optical communication devices is driving demand for optical circuits (High et al. 2007). As a starting point, excitonic transistors were developed (High et al. 2007) along with excitonic integrated circuits (High et al. 2008). These devices use an electric gate voltage to control exciton flow. Extending this work, Kuznetsova et al. (2010b) created an all-optical exciton transistor that used a laser beam to control exciton flow. This design is limited by high energy dissipation and low on-off ratio. In this chapter, we present an improved device that minimizes energy dissipation and features a high on-off ratio.

Optical control of exciton fluxes is realized for indirect excitons in a crossed-ramp excitonic device. The device demonstrates experimental proof of principle for all-optical excitonic transistors with a high ratio between the excitonic signal at the optical drain and the excitonic signal due to the optical gate. The device also demonstrates experimental proof of principle for all-optical excitonic routers.

3.2 Realization

We study indirect excitons in a crossed-ramp excitonic device. The indirect exciton energy band diagram is shown in Fig. 3.1a. A potential energy gradient—a ramp—is created by a shaped electrode at constant voltage with no energy-dissipating voltage gradient (Leonard et al. 2012). The design utilizes the ability to control exciton energy by electrode density (Kuznetsova et al. 2010a). An electrode on the sample surface—the top electrode (Figs. 3.1b, c and 3.2a, e)—is shaped so

J. Leonard, *Exciton Transport Phenomena in GaAs Coupled Quantum Wells*,
Springer Theses, https://doi.org/10.1007/978-3-319-69733-8_3

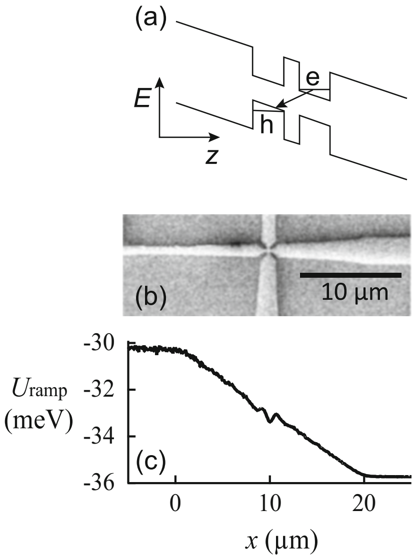

Fig. 3.1 Optically controlled excitonic transistor design. (**a**) Energy diagram showing coupled quantum wells with an applied electric field along the z-axis. Arrow indicates the electron and hole are in a bound state. (**b**) An SEM image of 1 arm of the crossed-ramp electrode aligned with (**c**) the simulated potential for indirect excitons along that arm

that a voltage applied between it and a homogeneous bottom electrode creates two crossing ramps. In each of these ramps, narrowing of the top electrode reduces F_z due to field divergence near the electrode edges and, as a result, increases the exciton energy. The electrode shape (Fig. 3.1b) is designed to obtain a constant potential energy gradient for indirect excitons in the CQW along each of the crossing ramps (Fig. 3.1c). At the crossing point, the electrodes are narrowed to compensate for the otherwise increased electrode density and thus to keep the exciton energy linear along both ramps (Kuznetsova et al. 2010a). Each of the two ramps is surrounded by flat-energy channels where the electrode width and, in turn, the energy of indirect excitons is constant (Figs. 3.1b, c and 3.2a, e). The parameters of the structure and experimental details are presented in Sect. 3.3.

The crossed-ramp excitonic device demonstrates experimental proof of principle for all-optical excitonic transistors with optical input, output, and control gate using indirect excitons as the operation medium. Photons transform into excitons at the optical input (source) and travel to the optical output (drain) due to the ramp potential. The output signal of the exciton emission in the drain region is controlled by a gate beam.

3.3 Experimental Methods

The CQW structure is described in Sect. 1.4. Unless otherwise indicated, excitons are photoexcited by a 633 nm HeNe laser corresponding to a photon energy above the $Al_{0.33}Ga_{0.67}As$ barrier. In Figs. 3.4 and 3.5 excitons are photoexcited by a Ti:Sapphire laser tuned to 787.5 nm, corresponding to the photon energy at the direct exciton resonance. Experiments are performed at $T_{\mathrm{bath}} = 1.6\,\mathrm{K}$. For the data in this chapter, the voltage applied to the top electrode $V_e = -3\,\mathrm{V}$.

3.4 Results

Figure 3.2b, f shows the images of the emission of indirect excitons along the straight-path and turned-path of the crossed-ramp device when only the source beam is on. The corresponding spatial profiles of the indirect exciton emission intensity $I(x)$ are presented in Fig. 3.2d, h. The profile of the source beam is shown in Fig. 3.2h in dashed lines. The emission patterns show enhanced emission intensity around the excitation spot due to the inner-ring effect studied earlier (Ivanov et al. 2006; Hammack et al. 2009). The inner ring was explained in terms of exciton transport and cooling: the heating of the exciton gas by laser excitation reduces the occupation of low-energy optically active exciton states, in turn reducing the exciton emission intensity in the excitation spot. When excitons travel away from the excitation spot, they thermalize to the lattice temperature, and the occupation of low-energy optically active exciton states increases, in turn increasing the exciton emission intensity and forming a photoluminescence ring around the excitation spot (Ivanov et al. 2006; Hammack et al. 2009). Emission patterns also show the

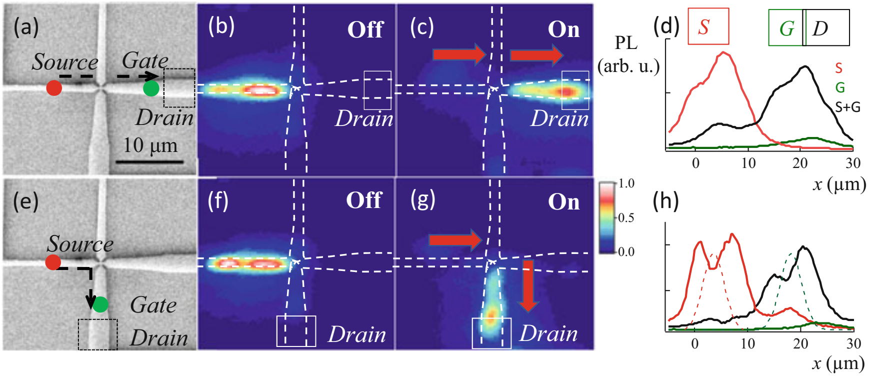

Fig. 3.2 Optically controlled excitonic transistor overview and operation. (**a**, **e**) SEM images of the electrode. The shaped electrode forms the crossing ramps for indirect excitons. Red and green circles indicate the excitation spots of the source (S) and gate (G) beam, respectively. Arrows indicate the straight-path (**c**) or turned-path (**g**) operation of the excitonic transistor. (**b**, **c**, **f**, **g**) Images of the exciton emission in (**b**, **f**) off and (**c**, **g**) on states for the straight-path (**b**, **c**) and turned-path (**f**, **g**) transistor operation. The power of the source beam $P_S = 0.5\,\mu\mathrm{W}$. The power of the gate beam $P_G = 0$ (**b**, **f**) and $0.2\,\mu\mathrm{W}$ (**c**, **g**). (**d**, **h**) Emission intensity of indirect excitons along the exciton flux for the straight-path (**d**) and turned-path (**h**) transistor operation in off state (red, $P_S = 0.5\,\mu\mathrm{W}$, $P_G = 0$), in on state (black, $P_S = 0.5\,\mu\mathrm{W}$, $P_G = 0.2\,\mu\mathrm{W}$), and when only the gate beam is on (green, $P_S = 0, P_G = 0.2\,\mu\mathrm{W}$). Spatial profiles of the source (red) and gate (green) excitation beam spots are shown as dashed lines in (**h**)

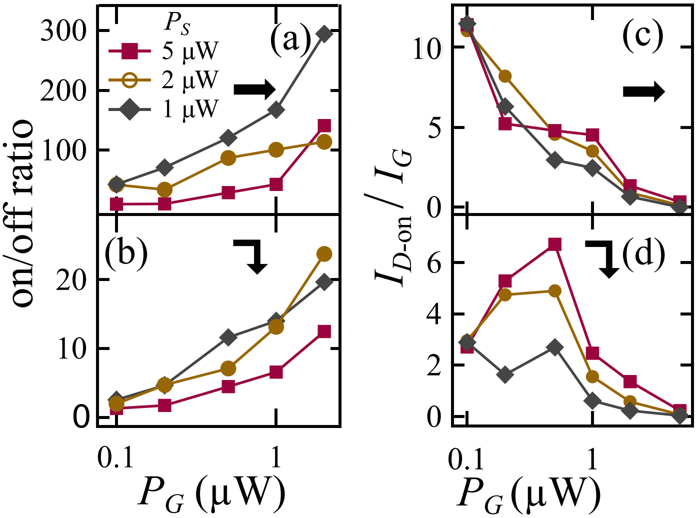

Fig. 3.3 Optically controlled excitonic transistor performance characterization. (**a**, **b**) The contrast ratio of the output intensity integrated over the drain region. (**c**, **d**) The ratio of the exciton emission intensity integrated over the drain region in on state to the exciton emission intensity integrated over the entire device when only the gate beam is on. The data are shown for the straight-path (**a**, **c**) and turned-path (**b**, **d**) operation of the excitonic transistor

enhanced emission intensity of indirect excitons at the lower energy side of the ramps due to exciton transport along the potential energy gradient.

The regime when only the source beam is on refers to off state of the excitonic transistor. The output signal of the transistor given by the emission of indirect excitons in the drain region is weak (Fig. 3.2b, f). The exciton signal in the drain region is controlled by an optical gate. The positions of the gate beam and drain region are shown in Fig. 3.2a, e for the straight-path or turned-path operation of the excitonic transistor, respectively. Figure 3.2c, g shows that turning on the gate beam strongly increases the exciton signal at the drain, switching the excitonic transistor to the on state. Figure 3.3a, b shows that the on/off ratio of the output intensity in the drain region reaches two orders of magnitude. Furthermore, even a weak gate beam generating a weak exciton signal (green lines in Fig. 3.2d, h) can strongly increase the output in the drain. Figure 3.3c, d shows that the ratio between the excitonic signal at the optical drain and the excitonic signal due to the optical gate $I_{D-\text{on}}/I_G$ reaches an order of magnitude. We note that the excitonic signal due to the optical gate is generally smaller than the gate signal since not all of the gate photons transform to the emitted photons due to losses, therefore, in general $I_{D-\text{on}}/I_G$ is not equal to the transistor gain.

The earlier studied exciton optoelectronic devices, where switching was controlled by gate voltage, demonstrated a switching time below 1 ns (High et al. 2007). Since no voltage switching is required for the all-optical excitonic transistors studied here, the switching time of these devices can potentially be even shorter. The study of signal kinetics in all-optical excitonic transistors is the subject for future work.

The crossed-ramp excitonic device also demonstrates an experimental proof of principle of all-optical excitonic routers. In the absence of the gate beam, the output signal of exciton emission is low in both ramps after the crossing point (Fig. 3.2b, f). Positioning the gate beam on one or another ramp of the crossed-ramp device determines the path where the output signal is directed (Fig. 3.2c, g). Even a weak gate beam generating a weak exciton signal can route a much stronger output signal of exciton emission (Fig. 3.2d, h).

3.5 Versatility

Qualitatively similar data are measured for the source and gate beam wavelengths 633 nm (Figs. 3.2 and 3.3) and 787.5 nm (Fig. 3.4). Furthermore, qualitatively similar data are measured for the crossed-ramp device (Figs. 3.2 and 3.3) and planar-electrode device, which forms a flat-energy channel (Fig. 3.5). In all these cases (1) the gate beam strongly increases the exciton signal at the drain region and (2) even a gate beam, which generates a weak exciton signal, can strongly increase the output at the drain (Figs. 3.2, 3.3 and Figs. 3.4, 3.5). This indicates that all-optical excitonic transistors can operate at various source and gate beam wavelengths and various electrode geometries.

3.6 Theoretical Model

Indirect exciton transport in a 1D potential energy channel was modeled using the nonlinear transport equation introduced in Sect. 1.2 modified to include terms for the ramp potential and two laser excitation spots:

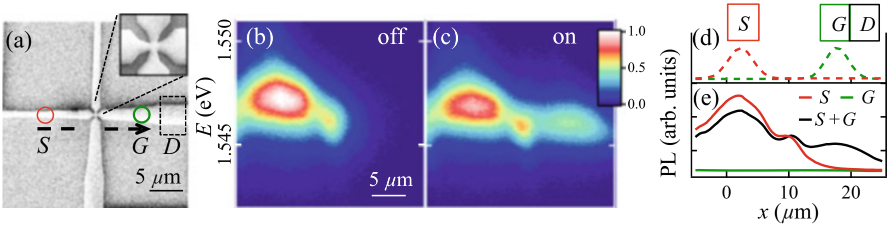

Fig. 3.4 Low laser energy optically controlled excitonic transistor overview and operation. (**a**) SEM images of the crossed-ramp device. Inset: SEM image of the crossing point of the crossed-ramp device. Red and green circles indicate the excitation spots of the source (*S*) and gate (*G*) beam, respectively. The arrow indicates the operation path of the excitonic transistor. (**b**, **c**) Energy-resolved images of the exciton emission in (**b**) off and (**c**) on states for the crossed-ramp transistor. The power of the source beam $P_S = 2\,\mu$W (**b**, **c**). The power of the gate beam $P_G = 0$ (**b**) and $2\,\mu$W (**c**). (**d**) Spatial profiles of the source (red) and gate (green) excitation beam spots. (**e**) Emission intensity of indirect excitons along the exciton flux for the crossed-ramp transistor in off state (red, $P_S = 2\,\mu$W, $P_G = 0$), in on state (black, $P_S = 2\,\mu$W, $P_G = 1\,\mu$W), and when only the gate beam is on (green, $P_S = 0$, $P_G = 1\,\mu$W). $V_e = -4$ V

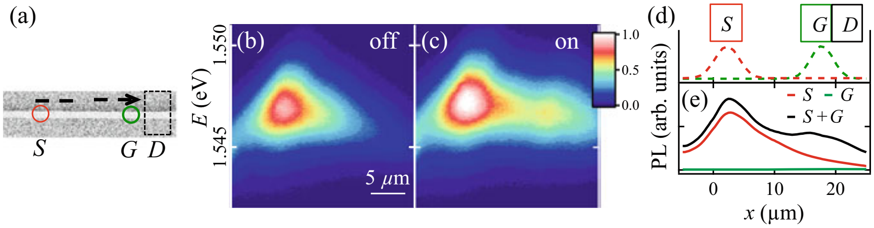

Fig. 3.5 Flat electrode optically controlled excitonic transistor overview and operation. (**a**) SEM images of the planar-electrode device. Red and green circles indicate the excitation spots of the source (S) and gate (G) beam, respectively. (**b**, **c**) Energy-resolved images of the exciton emission in (**b**) off and (**c**) on states for the planar-electrode transistor. The power of the source beam $P_S = 10\,\mu\text{W}$ (**b**, **c**). The power of the gate beam $P_G = 0$ (**b**) and $2\,\mu\text{W}$ (**c**). (**d**) Spatial profiles of the source (red) and gate (green) excitation beam spots. (**e**) Emission intensity of indirect excitons for the planar-electrode transistor in off state (red, $P_S = 10\,\mu\text{W}$, $P_G = 0$), in on state (black, $P_S = 10\,\mu\text{W}$, $P_G = 2\,\mu\text{W}$), and when only the gate beam is on (green, $P_S = 0$, $P_G = 2\,\mu\text{W}$). $V_e = -4\,\text{V}$

$$\nabla\left[D\nabla n + \mu n \nabla(u_0 n + U_{\text{ramp}})\right] - n/\tau + \Lambda_S + \Lambda_G = 0. \tag{3.1}$$

This equation was solved for the steady-state distribution of indirect excitons, n with $\nabla = \partial/\partial x$ (the coordinate x follows the path of the exciton flux along the energy channel and ramp). Diffusion and drift fluxes are given by the first and second terms in square brackets, respectively. The exciton diffusion coefficient D and mobility μ are related by the generalized Einstein relationship (Ivanov et al. 2006; Hammack et al. 2009), $\mu = D(e^{T_0/T} - 1)/(k_B T_0)$ where $T_0 = (\pi\hbar^2 n)/(2Mk_B)$ is the quantum degeneracy temperature and M is the exciton mass. The drift flux is due to the gradient in the applied ramp potential U_{ramp} (shown in Fig. 3.6d) and the exciton–exciton interaction. The exciton–exciton interaction was modeled as a repulsive dipolar interaction potential, approximated by $u_0 n$ with $u_0 = 4\pi de^2/\varepsilon_b$, where ε_b is the GaAs dielectric constant. The effect of the QW disorder potential is included in the diffusion coefficient, $D = D_0 \exp[-U_0/(u_0 n + k_B T)]$ (Ivanov et al. 2006; Hammack et al. 2009). Here, $U_0/2 = 0.5\,\text{meV}$ is the amplitude of the disorder potential and D_0 is the diffusion coefficient in the absence of disorder. This description includes (1) increased exciton localization to potential minima for decreasing temperature and (2) screening of the disorder potential for increasing exciton density (Ivanov et al. 2006; Hammack et al. 2009).

Optical generation of excitons at the source (gate) is given by $\Lambda_{S(G)}$. These have Gaussian profiles with position and FWHM chosen to match the experiment. The total injection rate of excitons is $R_{S(G)} = \delta y \int \Lambda_{S(G)}(x)dx$ where $\delta y \approx 1\,\mu\text{m}$ is the width of the potential energy channel. The exciton optical lifetime $\tau(T_0, T)$ determines the decay of optically active excitons (Ivanov et al. 2006; Hammack et al. 2009). The spatially varying exciton temperature used in Eq. (3.1) is found by solving a thermalization equation:

$$S_{\text{phonon}}(T_0, T) = S_{\text{pump}}(T_0, T, \Lambda_S + \Lambda_G, E_{\text{inc}}). \tag{3.2}$$

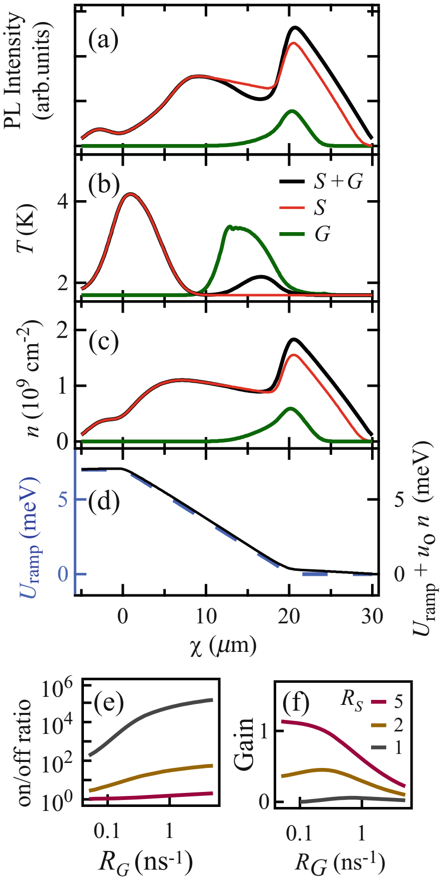

Fig. 3.6 Theoretical optically controlled excitonic transistor performance characterization. Exciton emission intensity (**a**), temperature (**b**), and density (**c**) for $R_S = 5\,\mathrm{ns}^{-1}$ and $R_G = 0$ (red, off state), $R_S = 0$ and $R_G = 0.5\,\mathrm{ns}^{-1}$ (green), and $R_S = 5\,\mathrm{ns}^{-1}$ and $R_G = 0.5\,\mathrm{ns}^{-1}$ (black, on state). (**d**) Bare ramp potential U_{ramp} (dashed blue) and screened ramp potential $U_{\mathrm{ramp}} + u_0 n$ for $R_S = 5\,\mathrm{ns}^{-1}$ and $R_G = 0.5\,\mathrm{ns}^{-1}$ (black). (**e**) The contrast ratio of the output intensity in the drain region vs. gate generation rate R_G for different source generation rates $R_S = 1$ (black), 2 (yellow), and 5 (red) ns^{-1}. (**f**) The gain of the excitonic transistor. The gain is defined as the ratio of the exciton emission intensity integrated over the drain region in on state to the exciton emission intensity integrated over the entire device when only the gate beam is on

Here, S_{phonon} accounts for energy relaxation of excitons due to bulk longitudinal acoustic phonon emission. S_{pump} is the heating rate due to the non-resonant laser excitation and is determined by the generation rates, $\Lambda_{S(G)}$ and the excess energy of photoexcited excitons E_{inc}. Expressions for S_{phonon}, S_{pump}, τ, and all other parameters of the model are given in Hammack et al. (2009).

The results of the simulations are presented in Fig. 3.6. Figure 3.6d shows the bare ramp potential U_{ramp} and the ramp potential screened by the exciton–exciton repulsion $U_{\mathrm{ramp}} + u_0 n$. Figure 3.6a–c shows the emission intensity, temperature, and density of indirect excitons. Figure 3.6e, f shows the contrast ratio of the output intensity in the drain region and the gain of the excitonic transistor for different source and gate powers.

Within the model, excitons generated in the gate area screen the disorder in the structure due to the repulsive dipolar interactions of indirect excitons. This increases the source exciton transport distance along the ramp, allowing excitons generated by the source laser to reach the drain region. The transport distance is further enhanced by the gate-beam-induced heating of the exciton gas due to the thermal activation of excitons in the disorder potential. The heating also increases the exciton lifetime that increases the density and, in turn, the screening of the disorder potential. The increasing exciton transport distance along the ramp generates the signal in the drain region. The features observed in the model are qualitatively similar to the experimental data, compare Fig. 3.2d, h with Fig. 3.6a, Fig. 3.3a, b with Fig. 3.6e, and Fig. 3.3c, d with Fig. 3.6f. However, the experimentally observed ratio between the excitonic signal at the optical drain to the excitonic signal due to the optical gate is much higher than the gain of the excitonic transistor calculated within the model. This indicates that a model beyond the considered drift/diffusion model should be developed for a quantitative description of the experimental data.

3.7 Summary

We report on experimental proof of principle for all-optical excitonic transistors with a high ratio of the excitonic signal at the optical drain to the excitonic signal due to the optical gate and experimental proof of principle for all-optical excitonic routers.

3.8 Further Reading

For background on exciton transistors we recommend reading High et al. (2007), for directional control of exciton fluxes (High et al. 2008). For an alternative version of an optical exciton transistor we recommend reading Kuznetsova et al. (2010b). For a look at optical transistors in polariton systems we recommend Gao et al. (2012).

References

M. Baldo, V. Stojanović, Optical switching: excitonic interconnects. Nat. Photon. **3**, 558–560 (2009)

T. Gao, P.S. Eldridge, T.C.H. Liew, S.I. Tsintzos, G. Stavrinidis, G. Deligeorgis, Z. Hatzopoulos, P.G. Savvidis, Polariton condensate transistor switch. Phys. Rev. B **85**, 235102 (2012)

A.T. Hammack, L.V. Butov, J. Wilkes, L. Mouchliadis, E.A. Muljarov, A.L. Ivanov, A.C. Gossard, Kinetics of the inner ring in the exciton emission pattern in coupled GaAs quantum wells. Phys. Rev. B **80**(15), 155331 (2009)

A.A. High, A.T. Hammack, L.V. Butov, M. Hanson, A.C. Gossard, Exciton optoelectronic transistor. Opt. Lett. **32**(17), 2466–2468 (2007)

A.A. High, E.E. Novitskaya, L.V. Butov, M. Hanson, A.C. Gossard, Control of exciton fluxes in an excitonic integrated circuit. Science **321**(5886), 229–231 (2008)

A.L. Ivanov, L.E. Smallwood, A.T. Hammack, Sen Yang, L.V. Butov, A.C. Gossard, Origin of the inner ring in photoluminescence patterns of quantum well excitons. Europhys. Lett. **73**(6), 920–926 (2006)

Y.Y. Kuznetsova, A.A. High, L.V. Butov, Control of excitons by laterally modulated electrode density. Appl. Phys. Lett. **97**(20), 201106 (2010a)

Y.Y. Kuznetsova, M. Remeika, A.A. High, A.T. Hammack, L.V. Butov, M. Hanson, A.C. Gossard, All-optical excitonic transistor. Opt. Lett. **35**(10), 1587–1589 (2010b)

J.R. Leonard, M. Remeika, M.K. Chu, Y.Y. Kuznetsova, A.A. High, L.V. Butov, J. Wilkes, M. Hanson, A.C. Gossard, Transport of indirect excitons in a potential energy gradient. Appl. Phys. Lett. **100**(23), 231106 (2012)

I.A. Young, E. Mohammed, J.T.S. Liao, A.M. Kern, S. Palermo, B.A. Block, M.R. Reshotko, P.L.D. Chang, Optical I/O technology for tera-scale computing. IEEE J. Solid State Circuits **45**, 235 (2010)

Chapter 4
Controlled Exciton Transport via a Conveyer

4.1 Introduction

This chapter presents an excitonic conveyer—a moving lattice created by a set of seven independently controlled electrodes controlled by AC voltages to create a moving sine wave potential. The excitonic conveyer realizes controlled transport of excitons as charge coupled devices (CCD) realize controlled transport of electrons (Smith 2010).

Moving potential lattices can be created by surface acoustic waves (SAW). Transport of excitons, exciton-polaritons, and laterally separated electrons and holes via SAW was intensively studied (Rocke et al. 1997; Rudolph et al. 2007; Lazic et al. 2010; Cerda-Méndez et al. 2010). The transport velocity in this case is defined by the sound velocity–SAW propagation speed $\sim 3\,\mu$m/ns. In contrast, the velocity of the electrostatic excitonic conveyer can be controlled by the AC frequency and can be from well below to well above the sound velocity.

4.2 Experimental Methods

The CQW structure is described in Sect. 1.4. The surface electrodes are described below.

Excitons are photoexcited by 788 nm Ti:Sp laser focused to a spot $\sim 5\,\mu$m in diameter. The exciton density is controlled by the laser excitation power P_{ex}. Photoluminescence (PL) images of the exciton cloud are taken by a CCD with a bandpass filter 810 ± 5 nm covering the spectral range of the indirect excitons. The diffraction-limited spatial resolution is $1.4\,\mu$m. The spectra are measured using a spectrometer with resolution 0.18 meV.

J. Leonard, *Exciton Transport Phenomena in GaAs Coupled Quantum Wells*,
Springer Theses, https://doi.org/10.1007/978-3-319-69733-8_4

The conveyer potential is created by a set of semitransparent 1 μm wide 120 nm thick indium tin oxide (ITO) electrodes on the sample surface. The distance between the electrode centers is 2 μm, the conveyer periodicity is seven electrodes, and the wavelength of the conveyer potential is $\lambda_{\text{conv}} = 14\,\mu$m. The conveyer electrodes are covered by a layer of transparent insulation (300 μm thick SiO_2). A set of connecting electrodes (10 μm wide 300 nm thick ITO) provides the contacts to the conveyer electrodes through $1 \times 10\,\mu$m etched openings in the insulating layer (Fig. 4.4b). The conveyer length is 380 μm, width is 80 μm.

The sample mounts in a He cryostat at 1.7 K. AC voltages to the conveyer electrodes are applied by coaxial cables with impedance-matching termination at the sample. The regime, where the indirect excitons have lower energy than spatially direct excitons in the CQW, is realized by DC bias $V_{\text{bias}} = 4$ V supplied separately. A set of differentially phase-delayed AC sinewaves at frequency f_{conv} creates a traveling potential lattice for indirect excitons—the excitonic conveyer. The amplitude of the conveyer potential for indirect excitons A_{conv} is controlled by the applied voltage. The conveyer velocity is controlled by the AC frequency $v_{\text{conv}} = \lambda_{\text{conv}} f_{\text{conv}}$. In order to apply AC frequencies to the sample we used a custom-designed sample holder called the Octopus.

Figure 4.1 presents photographs of the lower part of the insert Octopus for optics and RF electronics at cryogenic temperatures. The Octopus has eight broadband transmission lines providing up to eight independent channels. Both the sample and electronic circuit on PCB next to the sample are in superfluid He in the conveyer experiment.

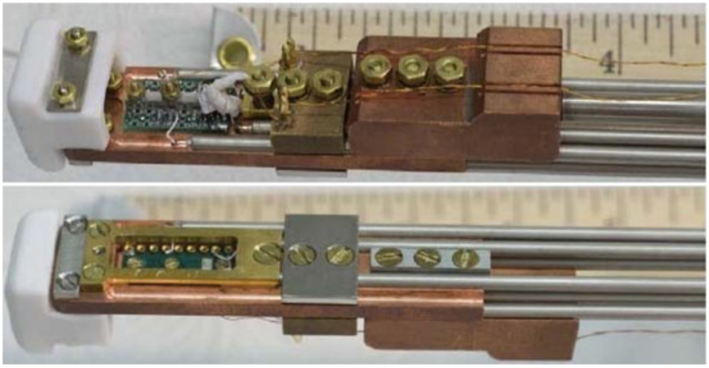

Fig. 4.1 Photographs of the radio frequency optical cryostat insert. The sample insert Octopus from two sides, an electronic circuit on PCB is seen on the upper photo and a socket for a sample is seen on the lower photo. The ends of the ~ 1 m long transmission lines are on the right

4.2.1 Circuit Schematic of the Conveyer RF System

AC voltages to the conveyer electrodes on the sample are delivered via seven broadband transmission lines with impedance-matching termination at the sample. We used coaxial cables UT-141B-SS silver-plated beryllium copper inner conductor, PTFE Teflon dielectric, and stainless-steel outer shell with diameter 3.6 mm, having a room-temperature attenuation of 3 dB/m at 10 GHz. The cable bandwidth complies with the frequency used in the experiments ($f_{\mathrm{conv}} = 50$–450 MHz), while the cable composition reduces heat conductance to the sample. The DC bias V_{bias} is supplied separately via regular wires. The transmission lines are capacitively terminated to block DC heating at the termination resistors. The circuit schematic for the conveyer RF system is presented in Fig. 4.2 for one of the channels and in Fig. 4.3 for the entire system with seven channels. The sample resistance between the top and bottom electrodes exceeds 10 MΩ in the experiments.

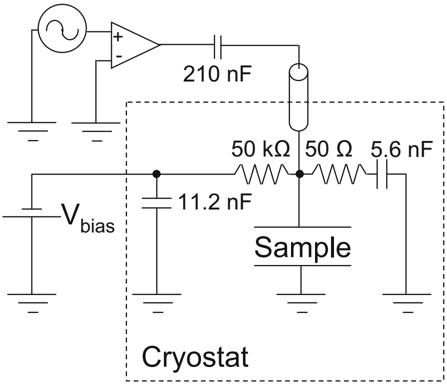

Fig. 4.2 Schematic of a single radio frequency circuit in the optical cryostat insert

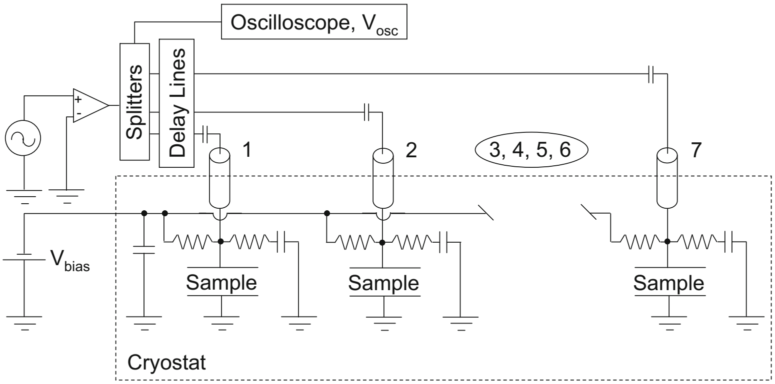

Fig. 4.3 Complete schematic of the radio frequency optical cryostat insert

4.3 Qualitative Results

Figure 4.4c–f shows x–y and x—energy PL images for conveyer off and on. The PL intensity profiles $I(x)$, obtained by the integration of the x—energy images over the emission wavelength, are shown in Fig. 4.4g, h. Exciton transport via conveyer is presented by the extension of the exciton cloud along the direction of the moving potential. We quantify it by the first moment of the PL intensity $M_1 = \int xI(x)dx / \int I(x)dx$, which characterizes the average transport distance of indirect excitons via conveyer. The spectrally broad emission at $x = 0$ (Fig. 4.4e, f) and sharp peak in $I(x)$ (Fig. 4.4g, h) originate from the bulk GaAs in the structure. To remove the contribution from the bulk, the shaded area is not included to the calculation of M_1 in the analysis of exciton transport.

4.4 Quantitative Analysis

This section presents quantitative measurements. To look at the data qualitatively, we calibrated the sample response to different frequencies using the method outlined in Sect. 4.4.1. In Sect. 4.4.2 we present quantitative results comparing different conveyer velocities.

4.4.1 Calibration of the Conveyer Amplitude

The conveyer amplitude is calibrated using the following procedure:

1. We applied AC voltage V_{osc} to all conveyer electrodes in phase and measured the spectral linewidth of indirect excitons. The linewidth, characterized by the half-width at half-maximum HWHM, has a contribution from the intrinsic linewidth of indirect excitons HWHM_0, which is present at zero voltage oscillation, and a contribution from the energy oscillation of indirect excitons $\mathrm{HWHM}_{\mathrm{osc}}$ due to the oscillating voltage. A defocused laser excitation with a spot $\sim 50\,\mu\mathrm{m}$ in diameter and $P_{\mathrm{ex}} = 220\,\mu\mathrm{W}$ was used. Figure 4.5a presents the measured HWHM as a function V_{osc} for one of the frequencies.
2. We subtracted in quadrature HWHM_0 from HWHM to obtain $\mathrm{HWHM}_{\mathrm{osc}}$ (Fig. 4.5a).
3. We performed numerical simulations of $\mathrm{HWHM}_{\mathrm{osc}}$ vs the amplitude of exciton energy oscillation. The comparison of these simulations to the experimental data allows determination of the amplitude of exciton energy oscillation. Figure 4.5b presents the obtained ratio between the AC voltage supplied to the transmission lines at the top of the cryostat V_{osc} and the amplitude of energy oscillation of

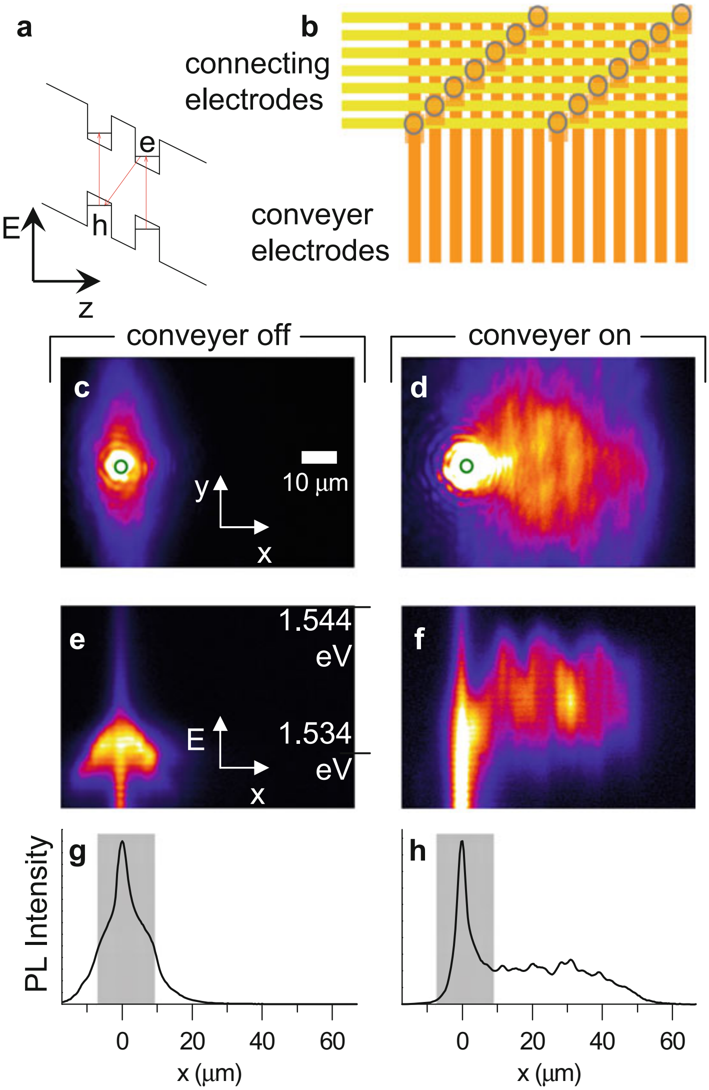

Fig. 4.4 Conveyer overview and operation. (**a**) CQW band diagram; e, electron; h, hole. (**b**) Electrode pattern, contacts are shown by circles. (**c**–**f**) x–y and x—energy PL images for conveyer off and on. (**g**, **h**) PL intensity profiles $I(x)$. $P_{ex} = 20\,\mu W$, $A_{conv} = 7.5\,meV$, $v_{conv} = 0.7\,\mu m/ns$

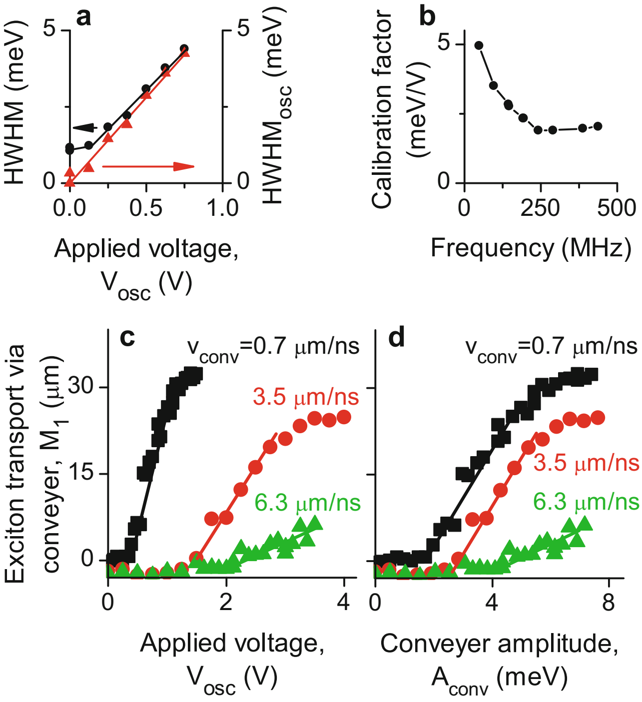

Fig. 4.5 Radio frequency optical cryostat insert and conveyer sample calibration. (**a**) AC voltage V_{osc} is applied to all conveyer electrodes in phase. Spectral linewidth of indirect excitons HWHM at 50 MHz vs V_{osc} (black points). The contribution from the energy oscillation of indirect excitons due to the oscillating voltage $\mathrm{HWHM}_{\mathrm{osc}} = [\mathrm{HWHM}^2 - \mathrm{HWHM}_0^2]^{1/2}$ vs V_{osc} (red triangles). Red line with slope m presents a linear fit with y-intercept fixed at 0. (**b**) The calibration curve for the conveyer amplitude: the ratio between the AC voltage supplied to the transmission lines at the top of the cryostat and the amplitude of energy oscillation of indirect excitons obtained from the simulations to fit the measured value of m vs driving frequency. (**c**, **d**) The average transport distance of indirect excitons via conveyer M_1 vs (**c**) the applied AC voltage at the top of the cryostat and (**d**) the conveyer amplitude

indirect excitons A_{conv} as a function of frequency. This is the calibration curve for the conveyer amplitude. Figure 4.5c, d shows the average transport distance of indirect excitons via conveyer M_1 as a function of V_{osc} and A_{conv}, respectively.

4.4.2 Quantitative Results

Figure 4.6 presents exciton transport via conveyer as a function of the conveyer amplitude A_{conv}. For a shallow conveyer, the exciton cloud extension M_1 is not affected by the conveyer motion indicating that the excitons do not follow the

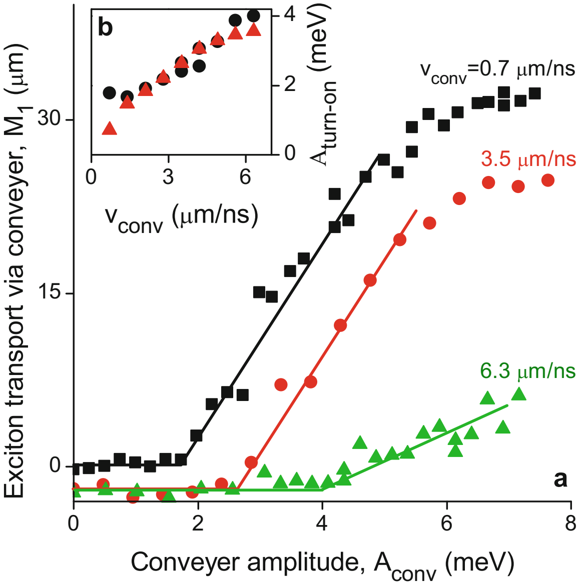

Fig. 4.6 Conveyer transport distance dependence on conveyer amplitude and conveyer velocity. (**a**) The average transport distance of indirect excitons via conveyer M_1 as a function of the conveyer amplitude, A_{conv}. Lines are a guide to the eye, $A_{turn\text{-}on}$ is A_{conv} at the line intersection. (**b**) The measured (black points) and calculated (red triangles) $A_{turn\text{-}on}$ vs the conveyer velocity. $P_{ex} = 20\,\mu W$

moving lattice, i.e. are dynamically delocalized in the lattice (Fig. 4.6a). In contrast, at higher conveyer amplitudes, excitons are moved by the moving lattice, i.e. are dynamically localized in the lattice. At the dynamical localization-delocalization transition (dLDT), the exciton cloud starts to follow the conveyer and M_1 changes from constant to increasing with A_{conv}. We define the conveyer amplitude at the dLDT, $A_{turn\text{-}on}$, as the point where the extrapolation of the growth of M_1 to small A_{conv} becomes equal to the low-A_{conv} constant. The dLDT is a dynamical counterpart of the LDT for excitons in static lattices (Remeika et al. 2009).

The control of f_{conv} gives an opportunity to study exciton transport via conveyers and in particular the dLDT as a function of the conveyer velocity. Figure 4.6 shows that exciton transport via conveyer is less efficient for higher v_{conv}. In particular, $A_{turn\text{-}on}$ increases with v_{conv}.

The control of P_{ex} gives an opportunity to study exciton transport via conveyers as a function of the exciton density. Figure 4.8a shows that excitons are hardly moved by the conveyer at low densities, efficient exciton transport via conveyer is achieved at intermediate densities, and exciton transport via conveyer becomes less efficient at high densities. The observed dependencies of exciton transport via conveyer on the exciton density and conveyer velocity and amplitude are compared to the theoretical model and discussed in Sect. 4.5.

4.5 Theoretical Model

The following nonlinear partial differential equation was used to model in-plane transport of indirect excitons subject to the applied conveyer potential $U_{\mathrm{conv}}(x)$:

$$\frac{\partial n_x}{\partial t} = \nabla \cdot [D_x \nabla n_x + \mu_x n_x \nabla (u_0 n_x + U_{\mathrm{conv}})] + \Lambda - \frac{n_x}{\tau_{\mathrm{opt}}}. \tag{4.1}$$

the first term in square brackets in Eq. (4.1) accounts for exciton diffusion, D_x is the diffusion coefficient. The second term accounts for exciton drift due to the dipole–dipole exciton interaction, which is approximated by $u_0 n_x$ (Ivanov 2002; Ivanov et al. 2010), and the conveyer potential $U_{\mathrm{conv}} = edF_{\mathrm{z}}(x) = ed\frac{\partial}{\partial z}V(\mathbf{r})$, where voltage $V(\mathbf{r})$ originates from the voltage applied to the conveyer electrodes $V_{\mathrm{z}=0}(x)$. The mobility μ_x is given by the generalized Einstein relationship $\mu_x = D_x(e^{T_0/T} - 1)/(k_B T_0)$, where $T_0 = (2\pi\hbar^2 n_x)/(M_x g k_B)$, $M_x \simeq 0.22\,m_0$ is the exciton mass, $g = 4$ is the spin degeneracy (Ivanov 2002). Due to the geometry of the system, we use the approximation $\nabla = \partial/\partial x$ and solve for the density of indirect excitons $n_x(x, t)$.

The effect of disorder intrinsic to QWs is included using a thermionic model for the diffusion coefficient, $D_x = D_x^{(0)} \exp\left(-U^{(0)}/(k_B T + u_0 n_x)\right)$ (Ivanov 2002). $D_x^{(0)}$ is the diffusion coefficient in the absence of QW disorder and $U^{(0)}/2$ is the amplitude of the disorder potential. The temperature of indirect excitons T is approximated as $T = T_{\mathrm{bath}}$. The non-resonant photoexcitation causes heating of the exciton gas by a few Kelvin. However, the hot excitons cool to the lattice temperature within a few microns of the excitation spot (Hammack et al. 2009) justifying the approximation.

The last two terms in Eq. (4.1) take account of the creation and decay of excitons. $\Lambda(x)$ is the generation rate and τ_{opt} is the optical lifetime. The increased exciton velocity due to transport via the conveyer can, in principle, shift the energy of excitons outside the photon cone and increase their optical lifetime. However, we evaluated τ_{opt} using the expressions given by Eqs. (1)–(6) in Hammack et al. (2009) and found that for the studied range of parameters, the corrections to the lifetime are small and can be neglected. Therefore we used a constant τ_{opt} independent of v_{conv}.

The results of the simulations are presented in Fig. 4.7. The green curve in Fig. 4.7a presents a snapshot of the conveyer potential for $n_x = 0$. The sinusoidal envelop of the conveyer potential with $\lambda_{\mathrm{conv}} = 14\,\mu\mathrm{m}$ is modulated by $2\,\mu\mathrm{m}$-period ripples, which originate from the finite spacing between the conveyer electrodes. The amplitude of these ripples can be controlled by the spacing between the conveyer electrodes d_{s} (the ripples essentially vanish for $d_{\mathrm{s}} < 0.5\,\mu\mathrm{m}$ for the structure). The repulsively interacting indirect excitons screen the external potential (Ivanov 2002). The snapshot of the exciton density distribution is shown by the red curve and the corresponding screened conveyer potential by the blue curve in Fig. 4.7a, b.

Fig. 4.7 Theoretical conveyer transport distance dependence on conveyer amplitude and conveyer velocity. (**a**, **b**) A snapshot of the conveyer potential (green), exciton density distribution (red), and corresponding screened conveyer potential (blue). PL intensity (black). $A_{\mathrm{conv}} = 8\,\mathrm{meV}$, $v_{\mathrm{conv}} = 0.7\,\mu\mathrm{m/ns}$. (**c**) M_1 vs A_{conv}. $D_x^{(0)} = 30\,\mathrm{cm}^2\,\mathrm{s}^{-1}$, $\Lambda = 10^9\,\mathrm{cm}^{-2}\,\mathrm{ns}^{-1}$, $\tau_{\mathrm{opt}} = 50\,\mathrm{ns}$

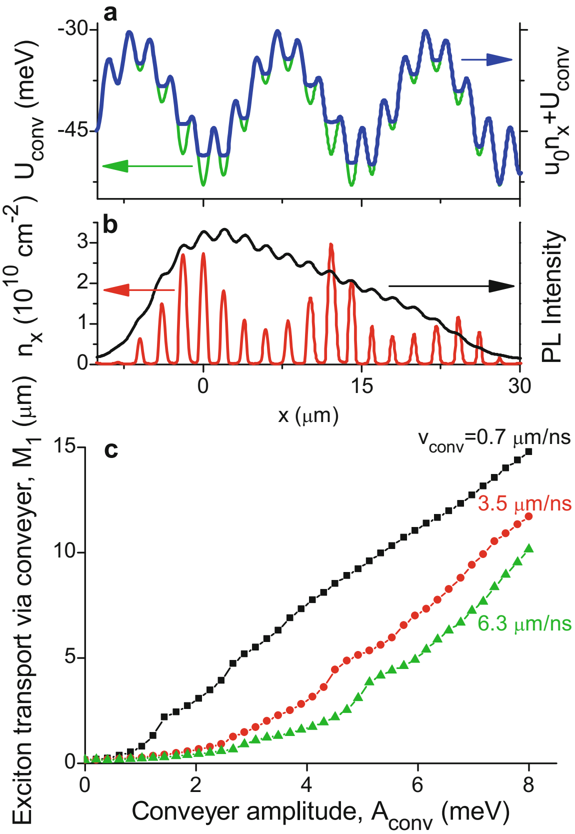

The time-integrated exciton PL with the spatial resolution taken into account is presented by the black curve in Fig. 4.7b. The average exciton transport distance via conveyer is evaluated by M_1, excluding the shaded area shown in Fig. 4.4g, h as for the experimental data. The obtained theoretical simulations of exciton transport via conveyer (Fig. 4.7c) are in qualitative agreement with the experimental data (Fig. 4.6) exhibiting the dynamical exciton delocalization in shallow conveyers and the dLDT with increasing conveyer amplitude. The simulated and measured conveyer amplitude at the dLDT, $A_{\text{turn-on}}$, are in qualitative agreement (Fig. 4.6b).

4.5.1 Conveyer Amplitude Dependence

Figures 4.6a and 4.7c show the conveyer amplitude dependence. When the conveyer amplitude is smaller than the exciton interaction energy or disorder amplitude, excitons are not localized in the minima of the moving conveyer potential, in analogy to the case of static lattices (Remeika et al. 2009), and therefore are not moved by the conveyer. When the conveyer amplitude becomes larger than both the exciton interaction energy and disorder amplitude, excitons can localize in the minima of the moving conveyer potential. This results in efficient transport of excitons via conveyer. The effect of the ripples in conveyer potentials on exciton transport is similar to that of disorder. More efficient exciton transport can be achieved by reducing the ripple amplitude. This can be realized by reducing d_s. The saturation of M_1 at large A_{conv} can be related to a device imperfections and can be studied in future works.

4.5.2 *Conveyer Velocity Dependence*

Figures 4.6a, b and 4.7c show the conveyer velocity dependence. Excitons can efficiently follow the moving conveyer potential when the maximum exciton drift velocity in the conveyer is higher than the conveyer velocity, $v_{\mathrm{drift}} = \mu_x(\partial U_{\mathrm{conv}}/\partial x)_{\max} \gtrsim v_{\mathrm{conv}}$. This leads to an estimate $A_{\text{turn-on}} \sim v_{\mathrm{conv}}\lambda_{\mathrm{conv}}/\mu_x$, qualitatively showing that a higher conveyer amplitude is required for efficient exciton transport via conveyer at a higher v_{conv}. The efficiency of exciton transport via conveyers can be improved by increasing μ_x. This can be achieved by reducing d_s and, in turn, $U^{(0)}_{\mathrm{ripple}}$.

A monotonic dependence of $A_{\text{turn-on}}$ on v_{conv} without abrupt changes at the sound velocity is consistent with the thermal velocity of excitons, $\sqrt{2k_BT/M_x} \sim 15\,\mu\mathrm{m/ns}$ at $T = 1.7\,\mathrm{K}$, is much higher than the sound velocity.

4.5.3 *Density Dependence*

Figure 4.8 shows the conveyer density dependence. At low densities, the excitons are localized in local minima of the disorder potential (given by the intrinsic disorder and ripples in the conveyer potential) and hardly follow the moving conveyer. At the intermediate densities, excitons effectively screen the disorder and can be efficiently moved by the conveyer. Exciton transport via conveyer becomes less efficient at the high densities when excitons screen the conveyer potential. The requirement for efficient exciton transport via conveyers $\mu_x(\partial U_{\mathrm{conv}}/\partial x)_{\max} \gtrsim v_{\mathrm{conv}}$ is relevant, where screening of disorder results in the enhancement of μ_x while screening of the conveyer potential results in the reduction of the conveyer amplitude.

In order to simplify these calculations for the analysis of the exciton density dependence, we approximate the conveyer potential by a cosine function $U^*_{\mathrm{conv}} = \Delta + A_{\mathrm{conv}}\cos(2\pi(x/\lambda_{\mathrm{conv}} - f_{\mathrm{conv}}t))$ and treat the ripples in the same way as the disorder potential. The position of the ripples is fixed, similar to the position of the CQW disorder potential. We approximate the effect of the CQW disorder and conveyer ripples on exciton transport within the thermionic

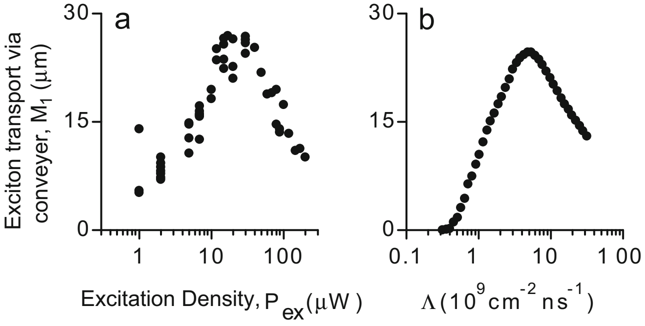

Fig. 4.8 Experimental and theoretical conveyer transport distance dependence on exciton density. (**a**) The measured and (**b**) calculated average transport distance of indirect excitons via conveyer M_1 as a function of exciton density. $A_{\text{conv}} = 4.9\,\text{meV}$, $v_{\text{conv}} = 0.7\,\mu\text{m/ns}$

model (Ivanov 2002) via the modification of the exciton diffusion coefficient $D_x = D_x^{(0)}\exp\left(-(U^{(0)} + U^{(0)}_{\text{ripple}})/(k_B T + u_0 n_x)\right)$. Here $U^{(0)}_{\text{ripple}}$ is the ripple amplitude obtained by simulations. $U^{(0)}_{\text{ripple}}$ is nearly proportional to U^*_{conv} and, therefore, it is approximated by $U^{(0)}_{\text{ripple}} = CU^*_{\text{conv}}$ (C is a fitting constant). The simulated density dependence of exciton transport via conveyer is in qualitative agreement with the experimental data (Fig. 4.8). Figure 4.9 presents details of the simulations for the density dependence of exciton transport via conveyer.

4.6 Summary

We report on the realization of electrostatic conveyers for excitons and experimental and theoretical studies of exciton transport via conveyers.

4.7 Further Reading

We recommend reading the Nobel Lecture (Smith 2010) because it forms the basis for many of the ideas in this paper, in addition to the basis for modern digital cameras. P.V. Santos studies controlled exciton transport using surface acoustic waves, we particularly recommend (Violante et al. 2014). Finally, Hasling et al. (2015) show the versatility of this method of exciton control.

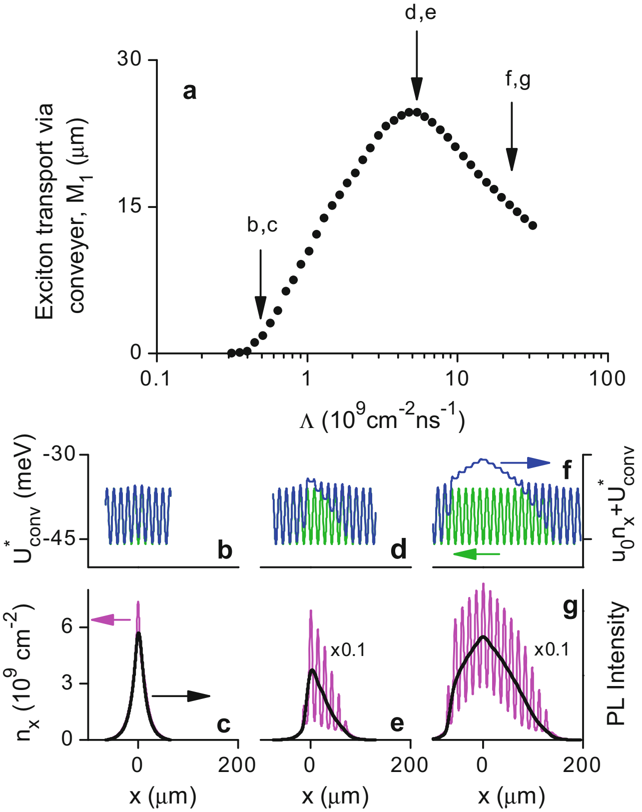

Fig. 4.9 Simulation details for the density dependence of exciton transport via conveyer. (**a**) Calculated average transport distance of indirect excitons via conveyer M_1 as a function of exciton generation rate. (**b–g**) A snapshot of the conveyer potential U^*_{conv} (green), exciton density distribution (magenta), and corresponding screened conveyer potential (blue). Time-integrated PL intensity (black). $\Lambda = 0.51 \cdot 10^9$ (**b**, **c**), $5.4 \cdot 10^9$ (**d**, **e**), and $22 \cdot 10^9 \mathrm{cm}^{-2}\,\mathrm{ns}^{-1}$ (**f**, **g**). $A_{\mathrm{conv}} = 4.9\,\mathrm{meV}$, $v_{\mathrm{conv}} = 0.7\,\mu\mathrm{m/ns}$

Acknowledgements In memory of Alexei Ivanov.

References

E.A. Cerda-Méndez, D.N. Krizhanovskii, M. Wouters, R. Bradley, K. Biermann, K. Guda, R. Hey, P.V. Santos, D. Sarkar, M.S. Skolnick, Polariton condensation in dynamic acoustic lattices. Phys. Rev. Lett. **105**, 116402 (2010)

A.T. Hammack, L.V. Butov, J. Wilkes, L. Mouchliadis, E.A. Muljarov, A.L. Ivanov, A.C. Gossard, Kinetics of the inner ring in the exciton emission pattern in coupled GaAs quantum wells. Phys. Rev. B **80**(15), 155331 (2009)

M.W. Hasling, Y.Y. Kuznetsova, P. Andreakou, J.R. Leonard, E.V. Calman, C. Dorow, L.V. Butov, M. Hanson, A.C. Gossard, Stirring potential for indirect excitons. J. Appl. Phys. **117**, 023108 (2015)

A.L. Ivanov, Quantum diffusion of dipole-oriented indirect excitons in coupled quantum wells. Europhys. Lett. **59**(4), 586–591 (2002)

A.L. Ivanov, E.A. Muljarov, L. Mouchliadis, R. Zimmermann, Comment on "Photoluminescence ring formation in coupled quantum wells: excitonic versus ambipolar diffusion". Phys. Rev. Lett. **104**(17), 179701 (2010)

S. Lazic, P.V. Santos, R. Hey, Exciton transport by moving strain dots in GaAs quantum wells. Physica E Low Dimens. Syst. Nanostruct. **42**(10), 2640–2643 (2010)

M. Remeika, J.C. Graves, A.T. Hammack, A.D. Meyertholen, M.M. Fogler, L.V. Butov, M. Hanson, A.C. Gossard, Localization-delocalization transition of indirect excitons in lateral electrostatic lattices. Phys. Rev. Lett. **102**(18), 186803 (2009)

C. Rocke, S. Zimmermann, A. Wixforth, J.P. Kotthaus, G. Böhm, G. Weimann, Acoustically driven storage of light in a quantum well. Phys. Rev. Lett. **78**, 4099–4102 (1997)

J. Rudolph, R. Hey, P.V. Santos, Long-range exciton transport by dynamic strain fields in a GaAs quantum well. Phys. Rev. Lett. **99**, 047602 (2007)

G.E. Smith, Nobel lecture: the invention and early history of the CCD. Rev. Mod. Phys. **82**, 2307–2312 (2010)

A. Violante, K. Cohen, S. Lazić, R. Hey, R. Rapaport, P.V. Santos, Dynamics of indirect exciton transport by moving acoustic fields. N. J. Phys. **16**, 033035 (2014)

Chapter 5
Observation of Exciton Spin Transport

5.1 Introduction

Spin devices may offer advantages such as low power dissipation, small size, and speed over charge based devices (Wolf et al. 2001; Awschalom and Flatté 2007). In addition, there are a variety of fundamental physics in electron based systems that can be explored in exciton based systems.

In this chapter, we report on the observation of the spin transport of spatially indirect excitons in GaAs coupled quantum wells (CQW). The spin relaxation time of indirect excitons is orders of magnitude longer than one of regular direct excitons. In combination with a long lifetime of indirect excitons, this makes possible spin transport of indirect excitons over substantial distances.

The spin dynamics of excitons can be probed by polarization resolved spectroscopy. In GaAs QW structures, the σ^+ (σ^-) polarized light propagating along the z-axis creates a heavy hole exciton with the electron spin state $s_z = -1/2$ ($s_z = +1/2$) and hole spin state $m_h = +3/2$ ($m_h = -3/2$). In turn, heavy hole excitons with $S_z = +1$ (-1) emit σ^+ (σ^-) polarized light. Excitons with $S_z = \pm 2$ are optically inactive. The polarization of the exciton emission $P = (I_+ - I_-)/(I_+ + I_-)$ is determined by recombination and spin relaxation processes. For an optically active heavy hole exciton, an electron or hole spin-flip transforms the exciton to an optically inactive state (Fig. 5.1) causing no decay of emission polarization. The polarization of emission decays only when both the electron and hole flip their spins. This can occur in the two-step process due to the separate electron and hole spin flips and the single-step process due to the exciton spin flip (Andreani and Bassani 1990; Maialle et al. 1993; Vinattieri et al. 1994).

J. Leonard, *Exciton Transport Phenomena in GaAs Coupled Quantum Wells*,
Springer Theses, https://doi.org/10.1007/978-3-319-69733-8_5

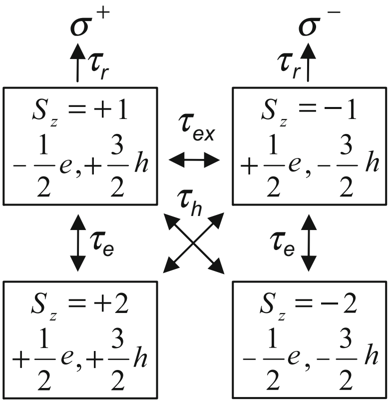

Fig. 5.1 Exciton spin flip pathways in GaAs. τ_r is the radiative recombination time, τ_e, (τ_h,) is the electron (hole) spin-flip time, τ_{ex} simultaneous electron-hole spin flip time. $\sigma^\pm$ indicates the polarization of emitted light. This model is described numerically in Eq. (5.2)

5.2 Exciton Spin Dynamics Without Transport

The dynamics of four exciton spin species with $S_z = \pm 2$ and $S_z = \pm 1$ are described by four coupled equations.

In the absence of exciton transport, the spin-flip model (Maialle et al. 1993) yields

$$\frac{d}{dt}\bar{n} = w\bar{n} \tag{5.1}$$

where w represents the possible spin flip pathways shown in Fig. 5.1 and numerically represented by

$$w = \begin{pmatrix} -(w_e^+ + w_h^+) & w_e^- & w_h^- & 0 \\ w_e^+ & -\begin{pmatrix} \frac{1}{\tau_r} + w_{\text{ex}} \\ +w_e^- + w_h^- \end{pmatrix} & w_{\text{ex}} & w_h^+ \\ w_h^+ & w_{\text{ex}} & -\begin{pmatrix} \frac{1}{\tau_r} + w_{\text{ex}} \\ +w_e^- + w_h^- \end{pmatrix} & w_e^+ \\ 0 & -w_h^- & w_e^- & (w_e^+ + w_h^+) \end{pmatrix}, \tag{5.2}$$

$\bar{n} = \left(n_{+2}\ n_{+1}\ n_{-1}\ n_{-2}\right)^T$, $w_{\text{ex}} = 1/(2\tau_{\text{ex}})$, $w_{e(h)}^\pm = \tau_{e(h)}^{-1}\left(1 + e^{\pm\Delta/k_BT}\right)$, τ_{ex} is the time for exciton flipping between $S_z = \pm 1$ states, τ_e and τ_h are the electron and hole spin flip times, τ_r is the exciton recombination time, and Δ is the splitting between the optically active $n_{\pm 1}$ and optically in-active (dark) $n_{\pm 2}$ states. For $\Delta \ll k_BT$, Eqs. (5.1) and (5.2) yield for the polarization of the exciton emission P and the relaxation time of the emission polarization τ_P

$$\tau_P^{-1} = 2\left(\tau_e^{-1} + \tau_h^{-1}\right) + \tau_{\text{ex}}^{-1} \tag{5.3}$$

$$\tau_P = \tau_r \frac{P}{1-P}. \tag{5.4}$$

5.3 Direct to Indirect Exciton Conversion

For the case of resonant excitation $\bar{\Lambda}$ is directly determined by the laser polarization. However, in the experiments reported in this paper the excitation was done at the energy of direct excitons, about 20 meV above the energy of indirect excitons. Such excitation has been chosen due to a high absorption coefficient at the direct exciton resonance, which allows creating a high exciton density with a low excitation power. For such excitation scheme, the generation rate of indirect excitons, $\bar{\Lambda}_{\text{indirect}} = \bar{n}_d/\tau_c$, where $\bar{n}_d$ is the density of direct excitons and τ_c is the direct to indirect exciton conversion time. The following estimations show that the polarization lost during the conversion time is small. Rate equation for the density of indirect excitons $\partial n_i/\partial t = n_d/\tau_c - n_i/\tau_r$ yields for the steady state $\tau_c = (n_d/n_i)\tau_r$. The experimental $n_d/n_i \sim 10^{-4}$ for the steady state and $\tau_r \sim 30$ ns (Butov et al. 1999) yield $\tau_c \sim 3$ ps. This is much smaller than the spin relaxation time and recombination time of direct excitons $\tau_{P,d} \sim 50$ ps and $\tau_{r,d} \sim 30$ ps (Maialle et al. 1993; Deveaud et al. 1991), hence the direct excitons convert into the indirect excitons before significant spin relaxation may occur, allowing the generation rate to be approximated by the laser polarization.

5.4 Phenomenological Model for Exciton Spin Transport

Combining the exciton spin relaxation Eq. (5.1) with the drift-diffusion equation yields the set of four coupled equations

$$\frac{\partial \bar{n}}{\partial t} = \nabla\left[D\nabla\bar{n} + \mu\bar{n}\nabla\left(u_0 n_{\text{total}}\right)\right] + w\bar{n} + \bar{\Lambda}, \tag{5.5}$$

where D is the exciton diffusion coefficient, μ is mobility, u_0 is the exciton interaction energy, $n_{\text{total}} = n_{-2} + n_{-1} + n_{+1} + n_{+2}$, and $\bar{\Lambda}$ is the generation rate of +1 excitons. This set of equations can be simplified in the case of fast spin relaxation of holes. In GaAs single QW, τ_h is in the range of tens of ps (Uenoyama and Sham 1990; Maialle et al. 1993; Vinattieri et al. 1994), much shorter than τ_e and τ_{ex} for the indirect excitons, so that $w_e, w_{\text{ex}} \ll w_h$. Also, the characteristic speed of exciton transport in the CQW is in the range of µm/ns (Hammack et al. 2007). Therefore, for the spatial averaging over lengths exceeding µm (which is the case in optical experiments due to the diffraction limit), hole spin flip takes place much faster than exciton diffusion, i.e. $\nabla\left[D\nabla\bar{n} + \mu\bar{n}\nabla\left(u_0 n_{\text{total}}\right)\right] \ll w_h\bar{n}$. These inequalities straightforwardly lead to the simplification of the set of Eqs. (5.5):

$$2\frac{\partial n_{+1}}{\partial t} = 2\nabla\left[D\nabla n_{+1} + \mu n_{+1}\nabla\left(u_0 n_{\text{total}}\right)\right] - \frac{1}{\tau_r}n_{+1} - \frac{1}{2\tau_P}\left(n_{+1} - n_{-1}\right) + \Lambda \tag{5.6}$$

$$2\frac{\partial n_{-1}}{\partial t} = 2\nabla\left[D\nabla n_{-1} + \mu n_{-1}\nabla\left(u_0 n_{\text{total}}\right)\right] - \frac{1}{\tau_r}n_{-1} - \frac{1}{2\tau_P}\left(n_{-1} - n_{+1}\right) \tag{5.7}$$

Both bright and dark exciton states are included in Eqs. (5.6), (5.7), however the fast hole spin flip process allowed the simplification of the set of four coupled equations for four exciton spin species Eqs. (5.5) to (5.6), (5.7), which contain only two bright exciton states $n_{\pm 1}$. For the estimations in the paper, we used the classical Einstein relationship $\mu = D/k_B T$ and approximated the exciton–exciton interaction by $u_0 = 4\pi^2 d/\epsilon$ as in Ivanov et al. (2006). Note that the spatially average polarization $\langle P\rangle = \langle\tau_P\rangle/(\langle\tau_P\rangle + \langle\tau_r\rangle)$ allows a rough estimate of τ_P without numerical simulations.

Rate equations combining the exciton spin relaxation equations (Maialle et al. 1993; Vinattieri et al. 1994) with the drift-diffusion equation (Ivanov et al. 2006) yield

$$2\frac{\partial n_{\pm 1}}{\partial t} = 2\nabla\left[D\nabla n_{\pm 1} + 2\mu n_{\pm 1}\nabla\left(u_0 n_b\right)\right] - \frac{1}{\tau_r}n_{\pm 1} - \frac{1}{2\tau_P}\left(n_{\pm 1} - n_{\mp 1}\right) + \Lambda\delta_{+,\pm}, \tag{5.8}$$

where D is the exciton diffusion coefficient, $\mu = D/k_B T$ mobility, u_0 interaction energy estimated by $u_0 = 4\pi^2 d/\epsilon$, $n_b = n_{+1} + n_{-1}$, and Λ generation rate of +1 excitons. Both bright and dark exciton states are included in Eq. (5.8), however the fast hole spin flip process allowed the simplification of the set of four coupled equations for four exciton spin species to the form of Eq. (5.8), which contain only two bright exciton states $n_{\pm 1}$. $n_{+1}(r)$, $n_{-1}(r)$, and $P(r)$ were calculated using Eq. (5.8) and compared to the experimental data.

The rate equations describing these processes (Maialle et al. 1993; Vinattieri et al. 1994) yield for the case when the splitting between $S_z = \pm 1$ and ± 2 states Δ is smaller than $k_B T$ the polarization of the exciton emission $P = \tau_P/(\tau_P + \tau_r)$ and the relaxation time of the emission polarization $\tau_P^{-1} = 2(\tau_e + \tau_h)^{-1} + \tau_{\text{ex}}^{-1}$, where τ_{ex} time for exciton flipping between $S_z = \pm 1$ states, τ_e and τ_h electron and hole spin flip times, and τ_r exciton recombination time. The requirement $\Delta \ll k_B T$ is typically fulfilled for indirect excitons. Indeed, for regular direct excitons in single GaAs QW, $\Delta \lesssim 100\,\mu\text{eV}$ (Ivchenko 2005). It is determined by the exchange interaction between the electron and hole in the exciton and scales $\propto \tau_r^{-1}$ (Andreani and Bassani 1990; Ivchenko 2005; Maialle et al. 1993; Vinattieri et al. 1994). For indirect excitons in the studied CQW, τ_r is about thousand times larger than for direct excitons (Butov et al. 1999) and therefore $\Delta \lesssim 100\,\text{neV} \ll k_B T$.

In GaAs single QW, τ_h and τ_{ex} are typically in the range of tens of ps and are much shorter than τ_e so that $\tau_P \approx \tau_{\text{ex}}$ (Uenoyama and Sham 1990; Maialle et al. 1993; Vinattieri et al. 1994). The short τ_{ex} results in fast depolarization of the exciton emission within tens of ps in GaAs single QW (Maialle et al. 1993; Vinattieri et al. 1994) making exciton spin transport over substantial distances problematic.

However, τ_{ex} is determined by the strength of the exchange interaction between the electron and hole. This gives an opportunity to control the depolarization rate by changing the electron-hole overlap, e.g. in QW structures with different QW widths or with an applied electric field (Maialle et al. 1993; Vinattieri et al. 1994).

The electron-hole overlap is drastically reduced in CQW structures. An indirect exciton in CQW is composed from an electron and a hole confined in different wells (Fig. 5.2). As a result of the small electron-hole overlap, the recombination time τ_r of indirect excitons is orders of magnitude longer than that of regular direct excitons and is typically in the range between tens of ns to tens of μs (Alexandrou et al. 1990). Long lifetimes of indirect excitons make possible their transport over large distances (Hagn et al. 1995; Larionov et al. 2000; Gärtner et al. 2006; Ivanov et al. 2006). However, the ability to travel is required yet insufficient condition for spin transport. Exciton spin transport over substantial distances also requires a long spin relaxation time. The small electron-hole overlap for indirect excitons should also result to a large $\tau_{\text{ex}} \propto \tau_r^2$ and in turn τ_P, thus making possible exciton spin transport over substantial distances.

5.5 Experimental Methods and Data

We probed exciton spin transport in a GaAs/AlGaAs CQW structure with two 8 nm GaAs QWs separated by a 4 nm $\text{Al}_{0.33}\text{Ga}_{0.67}\text{As}$ barrier (see sample details in Butov et al. (1999) where the same sample was studied), the band diagram of this structure is shown in Fig. 5.2. The electric field across the sample was controlled by an applied gate voltage V_g. The excitons were photoexcited by a cw Ti:Sapphire laser tuned to the direct exciton energy, $E_{\text{ex}} = 1.572\,\text{eV}$, and focused to a spot of $\sim 5\,\mu\text{m}$ in diameter. The spatial profile of the laser excitation spot was deduced from the profile of the bulk GaAs emission from the excitation spot. The excitation was circularly polarized (σ^+). The emission images in σ^+ and σ^- polarizations were taken by a CCD camera with an interference filter 800 ± 5 nm, which covers the spectral

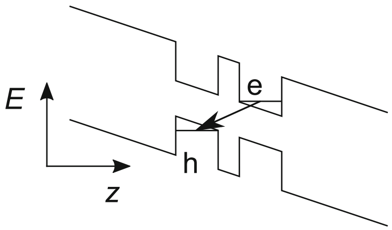

Fig. 5.2 Indirect Exciton Band Diagram. Energy diagram showing coupled quantum wells with an applied electric field along the z-axis. Arrow indicates the electron and hole are in a bound state. Electrons will move to the lower energy quantum well, holes to the higher energy quantum well. The quantum wells are positioned near each other so the electron and hole can bind together into an exciton. The spatial separation results in a large increase of exciton lifetime

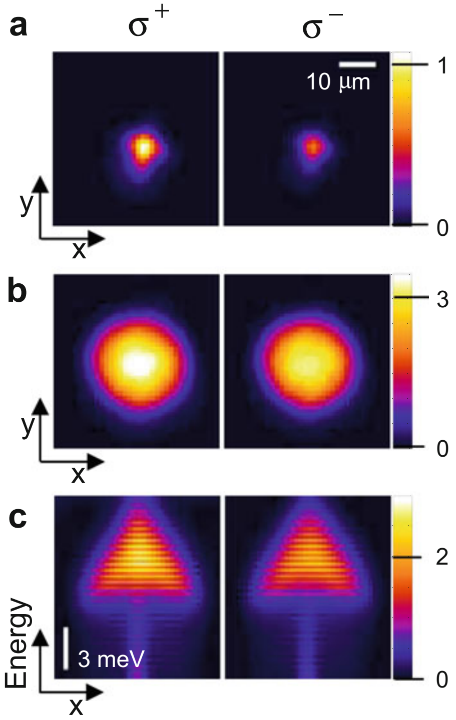

Fig. 5.3 Spin transport raw data. x–y images of the PL intensity of indirect excitons in σ^+ and σ^- polarizations for (**a**) $P_{\text{ex}} = 4.7\,\mu\text{W}$ and (**b**) $P_{\text{ex}} = 310\,\mu\text{W}$; $V_g = -1.1$ V, $E_{\text{ex}} = 1.582\,\text{eV}$. (**c**) Energy–$x$ images of the PL intensity of indirect excitons in σ^+ and σ^- polarizations; $V_g = -1.1$ V, $E_{\text{ex}} = 1.572\,\text{eV}$, $P_{\text{ex}} = 140\,\mu\text{W}$

range of the indirect excitons. The spatial resolution was $1.4\,\mu\text{m}$. The spectra were measured using a spectrometer with a resolution of 0.3 meV. The characteristic x–energy spectra and x–y images are shown in Fig. 5.3a–c. The exciton density n was estimated from the energy shift as in Ivanov et al. (2006). For recent discussions of the exciton–exciton interaction strength and the exciton density estimation, see Schindler and Zimmermann (2008); Remeika et al. (2009). We note that the results on exciton spin transport reported here are practically insensitive to the interaction strength.

5.6 Temperature Dependence

Increasing the temperature leads to the increase of the exciton cloud radius r_{cloud} and decrease of the circular polarization of exciton emission at the excitation spot center $P_{r=0}$ (Fig. 5.4a, b). The exciton cloud expansion $r_{\text{cloud}} \sim \sqrt{D\tau_r}$ is determined by the exciton diffusion coefficient D. The circular polarization of exciton emission $P = \tau_P/(\tau_P + \tau_r)$ is determined by the depolarization time of the emission τ_P. Therefore, the measurements of r_{cloud}, P, and τ_r allow estimating D and τ_P. D and τ_P were extracted from the measured r_{cloud}, $P_{r=0}$, and τ_r (Butov et al. 1999) via

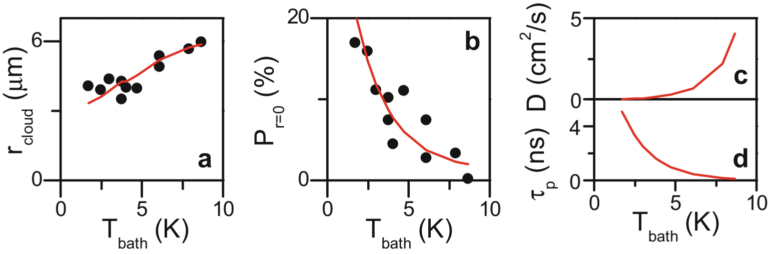

Fig. 5.4 Experimental and theoretical exciton spin polarization temperature dependence. Experimental (points) and simulated (curves) (**a**) exciton cloud radius and (**b**) degree of circular polarization at the exciton cloud center as a function of temperature. (**c**, **d**) Fit parameters—diffusion coefficient D and polarization relaxation time τ_P as a function of temperature

numerical simulations using Eq. (5.8). The obtained temperature dependencies for D and τ_P are plotted in Fig. 5.4c, d. The data show that (1) the depolarization time of the emission of indirect excitons reaches several ns, orders of magnitude longer than that of direct excitons in single QW (Maialle et al. 1993; Vinattieri et al. 1994), (2) the polarization rapidly decreases with increasing temperature, and (3) the decrease of polarization is correlated with the increase of the diffusion coefficient.

5.7 Density Dependence

Increasing the density leads to the increase of r_{cloud} and decrease of $P_{r=0}$ (Fig. 5.5a, b). At low densities, r_{cloud} is essentially equal to the excitation spot radius. Similar to the case of temperature dependence, these measurements of r_{cloud} and P allow estimating D and τ_P as a function of density. The measured r_{cloud} and $P_{r=0}$ were simulated using Eq. (5.8) with D and τ_P as fitting parameters. The obtained density dependencies for D and τ_P are plotted in Fig. 5.5c, d. The polarization degree of the exciton emission and the polarization relaxation time reduce with increasing density (Fig. 5.5b, d). Similar to the case of temperature dependence, the decrease of polarization is correlated with the increase of the diffusion coefficient. Figure 5.5e shows τ_P^{-1} vs D for the data in Fig. 5.5c, d.

5.8 Spatial Dependence: Exciton Spin Transport

Essential characteristics of the exciton spin transport are presented in Fig. 5.6a–c. Figure 5.6a shows the measured PL in σ^+ and σ^- polarization as a function of the distance from the excitation spot center r. Figure 5.6b shows the corresponding $n_{+1}(r)$ and $n_{-1}(r)$ calculated using Eq. (5.8) with D and τ_P in Fig. 5.5c, d. The polarization profiles are wider than the excitation spot that directly shows exciton

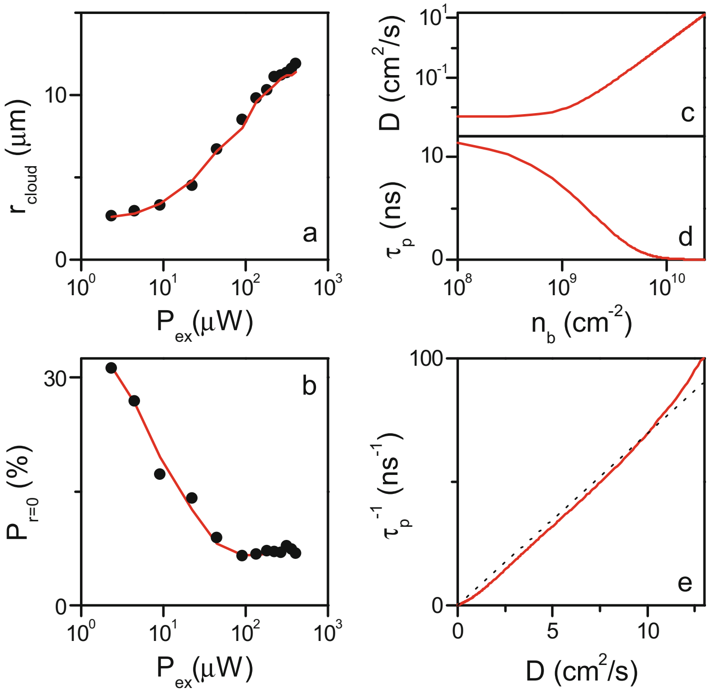

Fig. 5.5 Experimental and theoretical exciton spin polarization density dependence. Experimental (points) and simulated (curves) (**a**) exciton cloud radius and (**b**) degree of circular polarization at the exciton cloud center as a function of excitation density. (**c**, **d**) Fit parameters—diffusion coefficient D and polarization relaxation time τ_P as a function of $n_b = n_{+1} + n_{-1}$. (**e**) $1/\tau_P$ vs D

spin transport (Fig. 5.6c). The measured and calculated data on exciton spin transport are in agreement (Figs. 5.6c and 5.7a).

The polarization at HWHM of the exciton cloud P_{HWHM} is observed up to several microns away from the origin (Fig. 5.7a). This gives a rough estimate for the length scale of exciton spin transport. Figure 5.7a, b also shows P_{HWHM} and the spatially average polarization $\langle P \rangle$ calculated using Eq. (5.8) with D and τ_p in Fig. 5.5c,d obtained from fitting r_{cloud} and $P_{r=0}$ data in Fig. 5.5a, b.

The parameters used in the calculations of exciton spin transport D, τ_P, and τ_r were obtained from other experiments, different from exciton spin transport experiments: D—from exciton transport, τ_P—from emission polarization at the excitation spot center, and τ_r—from PL kinetics. The agreement between the calculated and measured data (Figs. 5.6 and 5.7) indicates that the major characteristics of exciton spin transport are determined by D, τ_P, and τ_r. The following assumptions were made in the model: (1) splitting between optically active and dark exciton states is small $\Delta \ll k_B T$, (2) hole spin flip is fast $\tau_h \ll \tau_e, \tau_{\mathrm{ex}}$ and $\nabla \left[D \nabla \bar{n} + \mu \bar{n} \nabla \left(u_0 n_{\mathrm{total}} \right) \right] \ll \bar{n}/(2\tau_h)$, and (3) conversion of the direct excitons into indirect excitons is fast $\tau_c \ll \tau_{P,d}$, see Sect. 5.3. The agreement between the

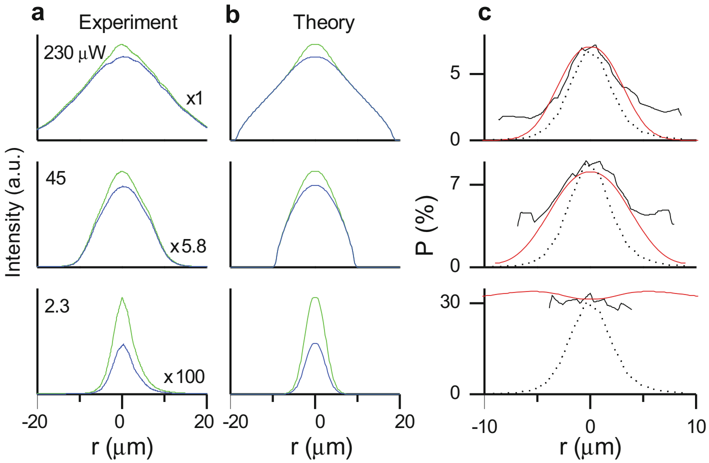

Fig. 5.6 Experimental and theoretical exciton spin polarization transport. (**a**) PL intensity of indirect excitons in σ^+ and σ^- polarizations (green and blue curves) as a function of r for $P_{\text{ex}} = 2.3, 45$, and $230\,\mu$W with estimated densities at $r = 0$ of $9 \cdot 10^8, 2 \cdot 10^{10}$, and $4 \cdot 10^{10}\,\text{cm}^{-2}$, respectively. (**b**) Simulated $n_{+1}(r)$ and $n_{-1}(r)$ for the same exciton densities as in (**a**). (**c**) Experimental (black curves) and simulated (red curves) PL polarization as a function of r for the same exciton densities as in (**a**, **b**). The profile of the bulk emission, which presents the excitation profile, is shown by dotted line. $T_{\text{bath}} = 1.7$ K. The simulations in (**a**, **b**, **c**) use $D(n)$ and $\tau_P(n)$ in Fig. 5.5c, d

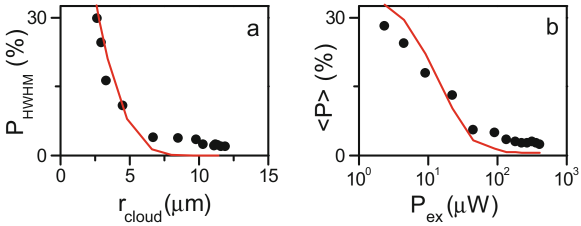

Fig. 5.7 Exciton spin polarization transport summary. (**a**) Experimental (points) and simulated (curve) polarization at HWHM of the exciton cloud P_{HWHM} as a function of r_{cloud}. (**b**) Experimental (points) and simulated (curve) spatially average polarization $\langle P \rangle$ as a function of excitation density. $T_{\text{bath}} = 1.7$ K. The simulations in (**a**, **b**) use $D(n)$ and $\tau_P(n)$ in Fig. 5.5c, d

experiment and the model (see Figs. 5.6 and 5.7) indicates that these assumptions are justified and the model accurately describes exciton spin transport (with roughly 20% uncertainty for the obtained dependencies of D and τ_P on temperature and density).

5.9 Discussion

Spin transport requires the ability of particles to travel maintaining spin polarization. This, in turn, requires large τ_r, D, and τ_P. Large τ_r and D are required to achieve exciton transport over substantial distances since the exciton diffusion length is determined by $\sqrt{D\tau_r}$, while large τ_P is required for maintaining spin polarization during the transport. Large τ_r is characteristic for indirect excitons for which it is orders of magnitude larger than for regular direct excitons. Large D is achieved with increasing exciton density (Fig. 5.5a, c). This behavior is consistent with the localization-delocalization transition: Excitons are localized at low densities due to disorder and delocalized at high densities when the disorder is screened by repulsively interacting indirect excitons (Ivanov et al. 2006; Remeika et al. 2009). Localized excitons do not travel beyond the excitation spot while delocalized excitons spread over the distance $\sim \sqrt{D\tau_r}$. This accounts for the density dependence of r_{cloud} and D (Fig. 5.5a, c). r_{cloud} and D also increase with temperature (Fig. 5.4), because of thermal activation of indirect excitons over maxima of the disorder potential.

For indirect excitons with a small electron-hole overlap $\tau_{\text{ex}} \propto \tau_r^2$ is large, $\tau_{\text{ex}} \gg \tau_e$, and $\tau_P \approx \tau_e/2$ so that the polarization relaxation is governed by the electron spin relaxation and, therefore, can be long. Indeed, τ_P for indirect excitons at low temperatures and low densities reaches 10 ns (Figs. 5.4d and 5.5d), much longer than τ_P for regular excitons, which is in the range of tens of ps (Maialle et al. 1993; Vinattieri et al. 1994). This orders of magnitude enhancement of the spin relaxation time for indirect excitons is achieved due to a small electron-hole overlap.

However, P and τ_P for indirect excitons drop with increasing temperature and density (Figs. 5.4 and 5.5). For qualitative understanding of this behavior we compare the variations of the polarization relaxation time and diffusion coefficient. Figures 5.4c, d and 5.5c, d show that τ_P^{-1} increases with D both when the temperature or density is varied. This behavior complies with the Dyakonov-Perel (DP) spin relaxation mechanism (D'yakonov and Perel' 1971) for which the spin relaxation time $\tau_{e,\text{ex}}^{-1} = \langle \Omega_{e,\text{ex}}^2 \tau \rangle$, where $\Omega_{e,\text{ex}}$ is the frequency of spin precession caused by the energy splitting between different spin states, $\tau \approx m_{\text{ex}} D/(k_B T)$ momentum scattering time, and m_{ex} exciton mass.

Figures 5.6c and 5.7a show that the length scale for exciton spin transport reaches several microns. It is large enough (1) for studying exciton spin transport by optical experiments, (2) for studying spin-polarized exciton gases in microscopic patterned devices, e.g. in in-plane lattices (Remeika et al. 2009), in which the period can be below a micron, and (3) for the development of spin-optoelectronic devices where *spin* fluxes of excitons can be controlled in analogy to the control of fluxes of unpolarized excitons High et al. (2008) (the distance between source and drain in the excitonic transistor High et al. (2008) was 3 μm; however, it is expected that the dimensions can be reduced below 1 μm by using e-beam lithography). The length scale for exciton spin transport exceeds the length scale for electron spin transport in metals where it is typically below 1 μm (Bass and Pratt, Jr. 2007).

The numerical model and measured data differ at large r (Figs. 5.6 and 5.7). This difference can originate from degrading experimental accuracy at large r where the polarization is obtained by the division of two small quantities $I_+ - I_-$ and $I_+ + I_-$. However, there are also physical processes which can contribute to this difference. The above phenomenological model can be improved by including the effect of a higher exciton temperature at the excitation spot center (Ivanov et al. 2006) and the spin Coulomb drag (D'Amico and Vignale 2001; Weber et al. 2005). The former should lead to a slower exciton spin relaxation at large r where the exciton gas becomes colder, while the latter would reduce the exciton spin diffusion coefficient D_s relative to D. Including these effects should make the modeling of the exciton spin transport more accurate.

Estimation of Spin Splitting The measured dependence $\tau_P^{-1}(D)$ can be used to estimate the spin splitting. For the splitting of electron states caused by the Dresselhaus mechanism (D'yakonov and Kachorovskiĭ 1986), which is the most likely scenario, $\Omega_e = 2\beta k/\hbar$ where k is the electron wave-vector. For the average thermal k of an electron in an exciton $k_T = \sqrt{2m_{\mathrm{ex}} k_B T/\hbar^2} m_e/m_{\mathrm{ex}}$, one obtains $\tau_P^{-1} = 2\tau_e^{-1} = 16\beta^2 m_e^2 D/\hbar^4$ (m_e is electron mass) and the measured $\tau_P^{-1}(D)$ (Fig. 5.5e) leads to the estimate of the spin splitting constant $\beta \approx 25\,\mathrm{meV\,Å}$.

The value of β for $\langle 001\rangle$-oriented QW be can also roughly estimated as $\beta = \gamma_c\langle k_z^2\rangle \approx \gamma_c(\pi/a)^2$, where a is the extension of the electron wave function in the QW and $\gamma_c \approx 27.5\,\mathrm{eV\,Å}^3$ is the bulk GaAs Dresselhaus constant (D'yakonov and Kachorovskiĭ 1986). For the studied CQW structure with a confining potential of 8 nm width and 260 meV depth, we obtain $\beta \approx 20\,\mathrm{meV\,Å}$, in agreement with the experiment.

5.10 Summary

The spin transport of indirect excitons has been observed. It originates from a long spin relaxation time and long lifetime of indirect excitons. The phenomenological model for exciton spin transport is in agreement with the experiment.

5.11 Further Reading

The results of this experiment were confirmed in a recent paper by Finkelstein et al. (2017) that extends our understanding of indirect exciton spin dynamics into a lower density regime that is dominated by nuclear spin interactions. Kowalik-Seidl et al. (2010) explored how spin relaxation time can be extended by going to low densities. Andreakou et al. (2015) and Andreakou et al. (2016) explored time dynamics of indirect exciton polarization and the effects of an applied magnetic field. A paper by Stotz et al. (2005) used moving artificial quantum dots to transport spin polarization. High et al. (2013) studied indirect exciton spin polarization in the milliKelvin temperature regime.

References

A. Alexandrou, J.A. Kash, E.E. Mendez, M. Zachau, J.M. Hong, T. Fukuzawa, Y. Hase, Electric-field effects on exciton lifetimes in symmetric coupled GaAs/$Al_{0.3}Ga_{0.7}As$ double quantum wells. Phys. Rev. B **42**(14), 9225–9228 (1990)

P. Andreakou, S. Cronenberger, D. Scalbert, A. Nalitov, N.A. Gippius, A.V. Kavokin, M. Nawrocki, J.R. Leonard, L.V. Butov, K.L. Campman, A.C. Gossard, M. Vladimirova, Nonlinear optical spectroscopy of indirect excitons in coupled quantum wells. Phys. Rev. B **91**, 125437 (2015)

P. Andreakou, A.V. Mikhailov, S. Cronenberger, D. Scalbert, A. Nalitov, A.V. Kavokin, M. Nawrocki, L.V. Butov, K.L. Campman, A.C. Gossard, M. Vladimirova, Influence of magnetic quantum confined stark effect on the spin lifetime of indirect excitons. Phys. Rev. B **93**, 115410 (2016)

L.C. Andreani, F. Bassani, Exchange interaction and polariton effects in quantum-well excitons. Phys. Rev. B **41**(11), 7536–7544 (1990)

D.D. Awschalom, M.E. Flatté, Challenges for semiconductor spintronics. Nat. Phys. **3**, 153–159 (2007)

J. Bass, W.P. Pratt, Jr., Spin-diffusion lengths in metals and alloys, and spin-flipping at metal/metal interfaces: an experimentalist's critical review. J. Phys. Condens. Matter **19**(18), 183201 (2007)

L.V. Butov, A.A. Shashkin, V.T. Dolgopolov, K.L. Campman, A.C. Gossard, Magneto-optics of the spatially separated electron and hole layers in GaAs/$Al_xGa_{1-x}As$ coupled quantum wells. Phys. Rev. B **60**(12), 8753–8758 (1999)

I. D'Amico, G. Vignale, Spin diffusion in doped semiconductors: the role of Coulomb interactions. Europhys. Lett. **55**(4), 566 (2001)

B. Deveaud, F. Clerot, N. Roy, K. Satzke, B. Sermage, D.S. Katzer, Enhanced radiative recombination of free excitons in GaAs quantum wells. Phys. Rev. Lett. **67**(17), 2355–2358 (1991)

M.I. D'yakonov, V.Yu. Kachorovskiĭ, Spin relaxation of two-dimensional electrons in noncentrosymmetric semiconductors. Sov. Phys. Semicond. **20**, 110 (1986)

M.I. D'yakonov, V.I. Perel', Current-induced spin orientation of electrons in semiconductors. Phys. Lett. A **35**(6), 459–460 (1971)

R. Finkelstein, K. Cohen, B. Jouault, K. West, L.N. Pfeiffer, M. Vladimirova, R. Rapaport, Transition from spin-orbit to hyperfine dominated spin relaxation in a cold fluid of dipolar excitons. arXiv:1706.00861 (2017)

A. Gärtner, A.W. Holleitner, J.P. Kotthaus, D. Schuh, Drift mobility of long-living excitons in coupled GaAs quantum wells. Appl. Phys. Lett. **89**(5), 052108 (2006)

M. Hagn, A. Zrenner, G. Böhm, G. Weimann, Electric-field-induced exciton transport in coupled quantum well structures. Appl. Phys. Lett. **67**(2), 232–234 (1995)

A.T. Hammack, L.V. Butov, L. Mouchliadis, A.L. Ivanov, A.C. Gossard, Kinetics of indirect excitons in an optically induced trap in GaAs quantum wells. Phys. Rev. B **76**(19), 193308 (2007)

A.A. High, E.E. Novitskaya, L.V. Butov, M. Hanson, A.C. Gossard, Control of exciton fluxes in an excitonic integrated circuit. Science **321**(5886), 229–231 (2008)

A.A. High, A.T. Hammack, J.R. Leonard, S. Yang, L.V. Butov, T. Ostatnicky, A.V. Kavokin, A.C. Gossard, Spin texture in a cold exciton gas. Phys. Rev. Lett **110**(24), 246403 (2013)

A.L. Ivanov, L.E. Smallwood, A.T. Hammack, S. Yang, L.V. Butov, A.C. Gossard, Origin of the inner ring in photoluminescence patterns of quantum well excitons. Europhys. Lett. **73**(6), 920–926 (2006)

E.L. Ivchenko, *Optical Spectroscopy of Semiconductor Nanostructures* (Alpha Science International, Harrow, 2005)

K. Kowalik-Seidl, X.P. Vögele, B.N. Rimpfl, S. Manus, J.P. Kotthaus, D. Schuh, W. Wegscheider, A.W. Holleitner, Long exciton spin relaxation in coupled quantum wells. Appl. Phys. Lett. **97**, 011104 (2010)

A.V. Larionov, V.B. Timofeev, J. Hvam, K. Soerensen, Interwell excitons in GaAs/AlGaAs double quantum wells and their collective properties. Sov. Phys. JETP **90**(6), 1093–1104 (2000)

M.Z. Maialle, E.A. de Andrada e Silva, L.J. Sham, Exciton spin dynamics in quantum wells. Phys. Rev. Lett. **47**(23), 15776–15788 (1993)

M. Remeika, J.C. Graves, A.T. Hammack, A.D. Meyertholen, M.M. Fogler, L.V. Butov, M. Hanson, A.C. Gossard, Localization-delocalization transition of indirect excitons in lateral electrostatic lattices. Phys. Rev. Lett. **102**(18), 186803 (2009)

C. Schindler, R. Zimmermann, Analysis of the exciton-exciton interaction in semiconductor quantum wells. Phys. Rev. B **78**(4), 045313 (2008)

J.A.H. Stotz, R. Hey, P.V Santos, K.H. Ploog, Coherent spin transport through dynamic quantum dots. Nat. Mater. **4**, 585 (2005)

T. Uenoyama, L.J. Sham, Carrier relaxation and luminescence polarization in quantum wells. Phys. Rev. B **42**(11), 7114 (1990)

A. Vinattieri, Jagdeep Shah, T.C. Damen, D.S. Kim, L.N. Pfeiffer, M.Z. Maialle, L.J. Sham, Exciton dynamics in GaAs quantum wells under resonant excitation. Phys. Rev. B **50**(15), 10868–10879 (1994)

C.P. Weber, N. Gedik, J.E. Moore, J. Orenstein, J. Stephens, D.D. Awschalom, Observation of spin Coulomb drag in a two-dimensional electron gas. Nature **437**, 1330–1333 (2005)

S.A. Wolf, D.D. Awschalom, R.A. Buhrman, J.M. Daughton, S. von Molnár, M.L. Roukes, A.Y. Chtchelkanova, D.M. Treger, Spintronics: a spin-based electronics vision for the future. Science **294**, 1488–1495 (2001)